Riding the Wave: Unveiling the Conformational Waves from RBD to ACE2

Nikhil Maroli

Computational Biology Division, DRDO Center for Life Science, Bharathiar University Campus, Coimbatore 641046, Tamil Nadu, India

Corresponding author: scinikhil@gmail.com

Abstract

The binding affinity between angiotensin-converting enzyme 2 (ACE2) and the receptor binding domain (RBD) plays a crucial role in the transmission and re-infection of SARS CoV2. Here, microsecond molecular dynamics simulations revealed that point mutations in the RBD domain induced conformational transitions that determines the binding affinity between ACE2 and RBD. These induced structural changes or conformational waves propagate through the RBD domain, leading to changes in the orientation of both ACE2 and the RBD residues at the binding site. The ACE2 receptor shows significant structural heterogeneity, whereas its binding to the RBD domain indicates a much greater degree of structural homogeneity. We found that the receptor is more flexible in its unbound state, and the binding of RBD domains changes it through induced structural transitions. The structural heterogeneity observed in the ACE2 unbound form plays a role in the promiscuity of viral entry as it may allow the receptor to interact with various related and unrelated ligands. Furthermore, rigidity may be important for stabilizing the complex and ensuring the proper orientation of the RBD-binding interface with ACE2. The greater structural homogeneity observed in the ACE2-RBD complex revealed the effectiveness of neutralizing antibodies and vaccines that are primarily directed towards the RBD-binding interface. Binding of the B38 antibody revealed restricted conformational transitions in the RBD and ACE2 receptor due to tight binding of the monoclonal neutralizing antibody.

Introduction

The SARS-CoV2 is a positive-strain single-stranded RNA virus that is causing the ongoing coronavirus disease 2019 (COVID-19) pandemic. Its highly transmissible and pathogenic properties have led to high morbidity and mortality rates worldwide since its initial detection in December 2019 [1]. Earlier studies have demonstrated the crucial involvement of angiotensin-converting enzyme 2 (ACE2) receptor in facilitating viral infections [2-3]. The entry of virus particles is mediated by angiotensin-converting enzyme 2 that expressed on the surface of various organs of the human cell. The binding of the viral spike glycoprotein (S protein) and ACE2 determines transmissibility and replication in host cells [4-7]. The S protein initiates receptor binding at the S1 and S2 subunits, which then fuses and initiates attachment to the host membrane. The primary role of ACE2 is hydrolyze angiotensin 2, thereby lowering blood pressure. The receptor is mainly expressed in the alveolar epithelial cells of the lungs. To achieve a higher affinity for spike protein binding, ACE2 must maintain a receptor-accessible state with at least one upward conformation to avoid steric clashes that disrupt the binding process. SARS-CoV2 is rapidly spreading across the globe, with several new variants that exhibit a stronger affinity for the receptors. The lineage B.1.1.7 or N501Y.V1 was first detected in England and rapidly expanded to over 25 countries. Lineage B.1.351 or N501Y.V2 was discovered in South Africa and was responsible for most pandemics at the end of 2020 [8-9]. The new variants were named P.1 and P.501Y, respectively. V3 was detected in Brazil within the last few months, and all three variants showed high transmission and reduced efficacy of vaccines and neutralizing antibodies. Several experimental and theoretical studies have revealed that mutations result in higher binding affinity for ACE2-RBD [10-13]. Furthermore, the mutations E484K and K417N also showed a higher

binding affinity between the RBD and ACE2 [11]. Lineages B.1.617.2, G/452R. V3, 21A, and 21A/S: 478 K have been reported in more than 100 countries. In 2021, the emergence of lineage B.1.1.529, which contains multiple mutations in the spike proteins, resulted in increased transmissibility, immune system evasion, and resistance to vaccines.[14-16]. However, these mutations have been shown to cause fewer severe illnesses than in previously reported strains. Various COVID-19 vaccines have been developed; however, no proven therapeutic agents, such as drugs or antibody sera, have been established for the reduction and recovery of infected patients. Antibody serum-based therapy may aid the recovery of patients infected with the virus [17]. The binding of S protein to ACE2 causes conformational changes that leading to transition from a metastable prefusion state to a stable post-fusion state. Plant based molecules shows inhibition of receptor and several proteins in the pathway [18]. Currently, the only effective treatment option is symptomatic treatment; hence, the development of specific targeted drugs is crucial. Coronavirus 'WH-Human 1' proteomics sequences have recently become available as a result of metagenomic RNA sequencing of a patient in Wuhan. WH-Human 1 shares 89.1% of its DNA with a group of coronaviruses known as the SARS coronaviruses [19]. Potential inhibitory antibodies can be identified by scanning millions of antibody sequences and detecting neutralizing antibodies based on this sequence. Antibodies neutralize SARS-CoV-2 by binding to either the RBD or NTD, which disrupts the virus's interactions with the human angiotensin-converting enzyme 2 (ACE2). Nevertheless, the molecular-level mutational and conformational dynamics of the RBD and spike proteins have not been extensively studied. Our previous study showed that the mutation results in an allosteric conformational change in the RBD domain, thereby decreasing the number of hydrogen bonds formed at the ACE2-RBD interface [20]. The antibody attaches to the RBD and competes with the ACE2 receptor. It can also bind to several binding sites on the RBD and trigger

conformational changes that result in steric hindrance of ACE2 binding. It can also attach to the RBD and impede the conformational transition required for viral proteins to effectively enter or bind. Previous study have demonstrated that powerful antibodies interact with ACE2-RBD and spike glycoproteins, resulting in decreased binding affinity or transmissibility [21-22]. The mechanisms by which conformational dynamics are propagated to other protein regions, and how this knowledge can be used for the design of small-molecule drugs or therapeutic candidates, remain largely unexplored. In this study, we utilized microsecond all-atom simulations to investigate the conformational changes induced by multiple RBD mutants when bound to ACE2 receptors and elucidate how these changes are propagated to the receptor. In addition, we employed machine learning-adapted clustering of 10 μs all-atom simulations to explore the conformational dynamics of ACE2. Our study also demonstrated that the binding of the B38 monoclonal neutralizing antibody to the RBD domain restricted conformational fluctuations of ACE2-RBD complex. Overall, our findings provides new insights into the ACE2-RBD interaction and the role of mutations in controlling the conformational flexibility of the ACE2 receptor.

Materials and methods

Simulation set-up and all-atom molecular dynamics simulations

The three-dimensional structures of the ACE2 and RBD domains of SARS-CoV-2 were obtained from the protein data bank with PDB ID: 6M17 [23]. Mutations in the RBD domains were introduced using the Chimera software package [24], and all co-occurring molecules including water were removed from the crystal structure. All-atom molecular dynamics simulations were performed using the CHARMM36 force field and TIP3P water model [25-26]. Electrostatic interactions were calculated using the particle mesh Ewald method [27] and a Verlet cutoff distance of 1.4 nm was used for short-range repulsive and attractive interactions. The

temperature and pressure were maintained at 310 K and 1 bar using Nose-Hoover temperature coupling and the Parrinello-Rahman algorithm, respectively. The LINCS algorithm was used to constrain all the bond lengths [28], and simulations were performed for 1 μs with a time step of 100 ps. Equilibration was performed in both the NVT and NPT ensembles for 10 and 20 ns, respectively. Simulations were performed using GROMACS 2021 [29], and visualization was performed using the Chimera software package.

Steered MD and Umbrella Sampling

The potential of mean force (PMF) of ACE2-RBD and all mutants were obtained by pulling the RBD domain from ACE2 receptor. The simulation boxes were defined in a way that it satisfied the minimum image convention and pulled the RBD along the axis. Prior to that, the simulation system was equilibrated in NVT and NPT ensembles for 10 ns while keeping ACE2 as the reference group. Steered simulations were conducted using a harmonic spring constant of 1000 kJ/mol with a pulling rate of 0.001 nm/ps. The RBD was pulled to 5 nm, generating 500 frames. The one-dimensional PMF curves obtained for each mutant gives a ΔG corresponding to the binding energy. An umbrella sampling MD of 100 ns was performed for each window to obtain a smooth profile. Furthermore, the weighted histogram analysis method [30] was used to estimate the free-energy profile from umbrella sampling simulations. A total of 50 μs simulation was performed to obtain the binding energy of each ACE2-RBD variant.

Machine Learning

Simulation trajectories were used to cluster the structures using the k-means clustering algorithm [31]. This is a widely used unsupervised machine-learning method for the segregation of a set of data points. Each frame is iteratively assigned to its closest centroid, and the centroids are updated until convergence achieved. The k-means function from the scikit-learn library was

used to perform k-means clustering on the protein coordinates extracted from the trajectory. Further, spectral clustering [32] technique that relies on the eigenvectors and eigenvalues of a similarity matrix which constructed from the trajectories were used. The data were transformed into a lower-dimensional space using the eigenvectors and eigenvalues of the Laplacian matrix of the similarity matrix. To produce the final clustering, k-means clustering was used on the transformed information after selecting the first k eigenvectors with the largest eigenvalues.

Results and Discussion

To understand the structural transitions of the RBD and induced transitions in ACE2 receptor by utilizing microsecond all-atom molecular dynamics simulations. The stability of the mutants' conformation and the transformation of the conformational transitions through the proteins were also evaluated. Using 10 µs simulations, we assessed the ACE2 conformational transitions in its apo, closed, and RBD-bound state. Additionally, we reported the restricted conformational transitions of RBD upon binding with B38 neutralizing antibodies.

Conformational stability of Angiotensin-converting enzyme 2

Several mutations in the RBD have been shown to exhibit higher affinity towards ACE2 receptor, which increases the transmissibility of virus. To determine the underlying causes of this higher affinity, we conducted one-microsecond all-atom molecular dynamics simulations of both wild and mutant (alpha, alpha+, beta, gamma, delta, epsilon, kappa, lambda and omicron.) RBDs with ACE2. Understanding the structural influence of these mutations is crucial for characterizing binding patterns and conformational dynamics. Several studies have reported the binding nature

of ACE2-RBD using molecular dynamics simulations, and many have argued that strong interactions occur owing to hydrogen bonding and electrostatic interactions at the binding site. However, there are no studies on the 'conformational waves' across the RBD, which control ACE2-RBD affinity. The root mean square deviations of backbone atoms and root mean square fluctuations of Cα of the ACE2 receptor upon binding the wild type and mutants are shown in Figure S1 and S3a. Higher RMSD and RMSF were observed for the ACE2 receptor, which binds to the mutants. The average backbone deviations of ACE2 with wild RBD are found to be 0.23 nm whereas, mutants show higher value of 0.6 nm for alpha- and kappa mutants. The higher fluctuations in ACE2 receptors indicate that structural transformation or steric hindrance induces conformational transitions. These conformational changes induced by the binding of the mutant RBD were further investigated using principal component analysis. The PCA-based backbone atoms are denoted by the eigenvectors of the covariance matrix, which is argued by its coincident eigenvalue and the total concerted motion of the protein, and are correlated with the protein functions. Figure S4a depicts the motion along the first and second components of the ACE2 backbone atoms. Our primary interest was at the binding site and point mutation site to observe any conformational transitions. The alpha variants showed higher fluctuations in the region between 600-1700 atoms, which corresponds to the α-helix chain from Ser19-Asn103, which is involved in the binding of RBD. The Ser19-52Thr and 55Thr-82Met regions are primary α-helix bundle that interacts with the RBD and the N-terminal domain of the ACE2 receptor. These fluctuations can be categorized as primary fluctuations because they arise from direct interaction with the RBD domain. The beta and epsilon mutants shows higher fluctuations in the second domain Gln89-Gln102, which is the small helix bundle situated behind the binding site. These fluctuations are characterized as secondary fluctuations because they arise as a consequence of

primary fluctuations in the helix bundle of Ser19-52Thr and 55Thr-82Met. Further, the time evolution of secondary structural changes of ACE2 receptors was obtained from a one-microsecond simulation and is depicted in Figure S5. The initial conformation of ACE2 receptors showed stable dynamics and a transition from 63.3% helix, 3.7% sheet, 8.4% turn, and 24.7% coil to 60.7% helix, 3.5% sheet, 6.2% turn, 28.9% coil, and 0.7% 3-10 helix. The alpha variants shows the occasional transition of helix, coil, and bend between residues 200-300 as 57.1% helix, 3.6% sheet, 10.9% turn, 27.6% coil, and 0.9% 3-10 helix. These residues were situated near the N-terminal region of the RBD and shows less contact with ACE2. Secondary and tertiary structural transitions occur in these regions, resulting in higher fluctuations. The secondary structural changes in ACE2 receptors in the wild-type and mutant systems are provided in the Table S17. Transitions from the α-helix to occasional bend and turn, along with the formation of small β-sheets, were observed in all mutants. In addition, tertiary structural changes in the receptor were evaluated by constructing a minimum distance matrix (Figure S6). The kappa mutant showed the highest deviations in both RMSD matrices, but there were no significant variations in the distance matrix, indicating the possible tertiary structural stability of ACE2 upon binding to the RBD. This further indicates that the RMSD fluctuations of the backbone and PCA-based fluctuations of ACE2 receptors arise from minor secondary structural changes as well as fluctuations at the binding site. The formation of hydrogen bonds and salt bridges at the binding site of ACE2-RBD caused further structural fluctuations observed in the RMSD and PCA.

Conformational dynamics of receptor binding domain (RBD)

Understanding the conformational dynamics of the receptor-binding domain is crucial for deciphering the ACE2 binding mechanism. The structural stability was characterized by assessing the RMSD, Cα RMSF, and PCA-based fluctuations of the backbone atoms. Because mutations

occur in the RBD, higher structural fluctuations and conformational changes are prominent (Figure S2). RMSF of the Cα atoms shows a substantial increase in the mutant RBD as depicted in Figure S3b. It can be noted that the highest fluctuations were observed between the residues 104-157, which is at the binding site. All mutations showed rearrangement of residue side chains at the binding site and the formation of hydrogen bonds with ACE2 receptors. The formation of a higher hydrogen-bonding network at ACE2-binding sites are crucial for strong affinity [33]. The PCA-based backbone fluctuations of the RBD were obtained to understand specific fluctuations at the binding site (Figure S4b). The alpha mutations that represent N501Y shows a wide peak at the PCA backbone corresponding to the residues Glu354-Lys357. Interestingly, these residues were far from the binding site, as well as from N501Y. This suggests that point mutations at position 501 triggered conformational changes in the RBD, which propagated to other regions. The secondary structure showed 7.7% helix, 28.9% sheet, 17.5% turn, and 45.9% coil at the end of the simulation, corroborating this transformation. The starting conformation had 6.2% helix, 30.9% sheet, 17.5% turn, 42.3% coil, and 3.1% 3-10 helix, and the formation of minor helical structures further enhanced the conformational stability of the RBD (Figure S7 and S8). The Free-energy landscape (FEL) obtained from the first two principal components of PCA revealed increased structural stability in the presence of N501 mutations (Figure 1). The FEL showed broad and deep minima for the wild RBD, whereas the N501 mutation indicated the presence of multiple and evenly distributed minima, indicating the occurrence of various conformational changes in the RBD. This suggests fewer conformational transitions of the RBD upon binding to ACE2. The mutation E484K, along with N501Y, induces more conformational transitions and high fluctuations in the Phe373-Phe377 and Asp389-Cys391 regions, which is the opposite end of the binding site. We observed β-sheet formation along with occasional meta-states of coil-bend

transitions in these regions. The free energy landscape of the double mutant revealed the presence of several distinct wells, with three minima associated with the lowest fluctuations. Notably, the transition from single-point mutations to multiple mutations (beta to omicron) resulted in significant variations in the free-energy landscape, with multiple spikes in PCA to a single wide spike observed in the omicron mutant. The region Leu387-Leu390 shows the highest fluctuations for K417N, E484K, and N501Y; these triple mutants showed multiple transitions from α-helices to coils through random coils and bend regions. Higher transitions from the N-terminal region to the binding site indicate secondary structural changes in the mid-region of the RBD. The gamma variants with K417T, E484K, and N501Y mutations showed similar structural changes to RBD. However, 417T causes a significant loss in the α-helix and the formation of a bend and coil. The PCA-based backbone fluctuations were residue-specific, whereas the beta variants exhibited a wide range of fluctuations in the chain. The beta variant shows a 6.2% helix, 26.8% sheet, 22.2% turn, and 44.8% coil, whereas the gamma variant shows a 3.1% helix, 28.4% sheet, 20.6% turn, 45.9% coil, and 2.1% 3-10 helix. The transformation of α-helix to β-sheet or the loss of helical content changes the hydrogen bonding pattern between the residues in the RBD domains, which leads to higher fluctuations, as observed in RMSD and RMSF values. Furthermore, the free energy landscape of the beta mutant showed a wide and two minima, whereas alpha varients showed multiple minima with sharp peaks. The 417T mutation further stabilized the RBD domain through structural changes, as seen in the free energy landscape. This indicates a well-connected wide minima at the center of the FEL, as depicted in Figure 1. Kim et al reported the differential interaction of ACE2-RBD interactions and mutants of concern. Their study on alpha, beta, gamma, and delta variants showed higher pulling for the detachment of the RBD domain from ACE2 receptors due to N501Y mutations, in addition to the role of N90-glycan followed by beta, gamma,

and delta variants. They also reported a higher number of contact residues in RBD mutants with ACE2 receptors. Here, we observed a fluctuations in certain residues far from the mutation sites, which caused secondary structural changes in different parts of the receptor. The RBD domain, which interacts with the S2 domain, showed significant variations in alpha-helical content. It travels through proteins and imitates tight binding with the ACE2 receptor. The delta variant with L452R and T478K mutations at the binding site causes a maximum of 0.15 nm fluctuations, which is 70 % less than that of other variants. In the delta variant, 6.7% helix, 33.0% sheet, 19.1% turn, 38.1% coil, and 3.1% 3-10 helix content. As a result, the free energy landscape shows a single wild well with a single minimum that diverges from the wider well. Here, transformation from coil to bend and turn, along with occasional α-helices and β-sheets, was observed in the secondary structure. In the case of multiple mutations compared to a single mutation of L452R (epsilon), the secondary structure content demonstrated a 10.3% helix, 27.3% sheet, 17.5% turn, 42.8% coil, and 2.1% 3-10 helix. A greater loss of secondary structure was observed in the C-terminal regions of the RBD, with multiple minima spread across the principal components, as shown in Figure 1. The double mutations L452R and E484Q (kappa) could potentially have higher transmissibility and severity or reinfection risk and require continuous monitoring. Kappa mutations are reported to be highly contagious and have the ability to evade neutralization antibodies. The free energy landscape of the kappa variant showed a wide peak with the lowest energy and a single spike, as shown in Figure 1i. The variant showed a 6.2% helix, 29.4% sheet, 13.9% turn, 47.9% coil, and 2.6% 3-10 helix in its secondary structure and formed α-helix and turn region at the C-terminal region. The lambda variant with L452Q and F490S mutations also showed a similar two-peak FEL, but it was found that both peaks were moderately wide and multiple peaks were observed in the backbone atoms, especially in the region Tyr380-Phe400. The α-helix at the N-terminal region,

which is situated at the binding site of ACE2, undergoes a transformation to bend and turn. Multiple meta-states were also observed between the turn-coil bend, which resulted in a 6.7% helix, 30.9% sheet, 25.8% turn, and 36.6% coil in its secondary structure. The omicron mutation, which reported the highest number of mutations (G339D, S371L, S373P, S375F, K417N, N440K, G446S, S477N, T478K, E484A, Q493R, G496S, Q498R, N501Y, and Y505H) showed fluctuations in residues between Asn450-Thr500. The free energy landscape of the omicron variant showed wide and lowest minima among the mutants. It is also observed the transition of secondary structure to 9.3% helix, 32.6% sheet, 22.3% turn and 35.8% coil. It is evident that these mutations result in higher structural stability in the RBD domain. This is possible through conformational transitions and inter-residue interactions with ACE2 receptors. The mutations not only lead to higher affinity and transmissibility, but also transform the RBD to more energetically stable conformations, as observed in the free energy landscape. Interestingly, these mutations cause structural changes in the RBD, which is distant from the binding site as well as the mutation site.

ACE2-RBD interactions

The binding affinity between the angiotensin-converting enzyme 2 (ACE2) receptor and receptor-binding domain (RBD) is primarily driven by multiple intermolecular forces, including hydrogen bonding, electrostatic interactions, van der Waals forces, and salt bridges. The hydrogen-bonding network at the binding interface between wild-type ACE2 and RBD has been shown to consist of an average of nine hydrogen bonds, which contribute significantly to the stability of the complex (Figure S9a). However, upon analysis of the mutations, excluding the omicron variant, it was observed that the hydrogen-bonding network was reduced to an average of seven hydrogen bonds. In contrast, the omicron variant exhibited the highest (9-10) average number of hydrogen bonds. Initial crystal structure analysis of the ACE2-RBD complex revealed the presence of 10 hydrogen

bonds between residues: Ser19-Ala475, Gln24-Asn487, Lys31-Gln493, Glu35-Gln493, Glu37-Tyr505, Asp38-Tyr449, Tyr41-Thr500, Gln42-Gln498, Tyr83-Asn487, and Lys353-Gly502. These hydrogen bonds were found to have a maximum energy of 25 kJ/mol and total hydrogen bond energy of 196 kJ/mol. However, at the end of the simulation, residues Gln24-Asn487, Glu35-Gln493, Tyr-83-Asn487, Lys353-Gly502, and Asp355-Thr500 formed hydrogen bonds, with a total energy of 96 kJ/mol. The alpha mutation showed nine hydrogen bonds in the initial structure, similar to the wild type, but formed two hydrogen bonds with Lys353-Tyr501 and Lys353-Gln502. The final structure of alpha mutations showed three hydrogen bonds with a total energy of 51 kJ/mol, namely Ala475-Gln24, Asn487-Tyr83, and Gly502-Lys353. An additional mutation in the alpha+ increases the total hydrogen bond strength to 185.08 kJ/mol with the interactions such as Ser19-Ala475, Gln24-Asn487, Lys31-Gln493, Glu35-Gln493, Glu37-Tyr505, Tyr41-Thr500, Gln42-Gln498, Tyr83-Asn487 and Lys353-Tyr501. However, in the end, these hydrogen bonds are restricted to five residues (Ser19-Ala475, Glu35-Gln493, Tyr41-Thr500, Tyr83-Asn487, and Lys353-Gly502) with a total energy of 108 kJ/mol. The addition of the K417N mutation did not increase the hydrogen bond energy (149 kJ/mol). However, the initial structure possessed nine hydrogen bonds, including Ser19-Ala475, Glu37-tyr505, Asp38-Tyr449, Tyr41-Th500, Glnn42-Gln498, Tyr83-Asn487, Lys353-Tyr501, and Lys353-Gly502. These hydrogen bonds decreased at the end of the simulations (Ser19-Ala475, Glu37-tyr505, Asp38-Tyr449, Tyr41-Thr500, Gln42-Gln498, Tyr83-Asn487, Lys353-Tyr501, and Lys353-Gly502). The delta mutations show higher hydrogen bond energy for the both initial and final frame, the residues Ser19-Ala475, Lys31-gln493, Glu35-Gln493, Glu37-Tyr505, Asp38-Tyr449, Tyr41-Thr500, Gln42-Gl498, Tyrr83-Asn487 and Lys353-Gly502 and final structure shows hydrogen bond between the residues Ser19-Ala475, Gln24-Ala475, Lys31-Glu484, Tyr83-Asn487, Glu329-Arg439, Lys353-Gly502 and

Asp355-Thr500. When it moved from alpha to omicron, the residues that participated in the hydrogen bond patterns were similar. The mutation induces structural rearrangement, which reduces the distances between the hydrogen bond acceptor donors and increases the energy between these residues. The omicron mutations showed the lowest average distances between the residues to form hydrogen bonds between residues Ser19-Ala475, Gln24-Asn487, Asp38-Ser496, Asp38-tyr449, Tyr41-Thr500, Gln42-Arg498, Tyr83-Asn487, Lys353-Ser496, and Lys353-Gly502, with the highest energy of 230 kJ/mol (Figure S10 and S11). Interestingly, the native ACE2-RBD shows an average electrostatic interaction energy of -285 kJ/mol, whereas the omicron variants show -480 kJ/mol (Figure S10b). These significant differences in the electrostatic energy at the binding site arise because of the changes in the distance between the residues arising from structural rearrangements. The initial changes observed in the mutant static structure were consistent throughout the simulations. The collective movements of the Cα atoms of both RBD and ACE2 indicate conformational waves through the protein due to mutations at different sites. The movements in the RBD arise due to the mutations, while ACE2 fluctuations arise due to the induced conformational changes due to the strong binding of RBD. However, the average van der Waals interaction energies between ACE2-RBD were found to be lower for the mutants than for the wild type. The binding sites of ACE2 consist of charged, uncharged, and polar amino acids such as Ser19, Gln24, Lys31, Glu35, Glu37, Asp38, Tyr41, Gln42, Tyr83, Lys353, Ala475, Asn487, Gln493, Tyr505, Tyr449, Thr500, Gln498, Asn487, and Gly502 in RBD. The solvent-accessible surface area was found to increase from the alpha to omicron mutant, as depicted in the Figure S12-15. Here, we did not consider the water molecules and glycans present at the ACE2-RBD interface. Earlier reports provided the detailed interaction of interstitial water and how water molecules form hydrogen bonds with two proteins [34]. Studies have shown that spike glycans

have no impact on the binding of the RBD to ACE2 [35]. There are two glycosylation sites on the spike RBD of CoV-2, located at residues 331 and 343, respectively, both of which are removed from the spike-ACE2 interface. Notably, these positions experience extensive diversity in the complex glycosylation carried out by ER- and Golgi-resident processing enzymes, indicating that whatever function they may have indirectly influenced spike-ACE2 interfaces is unlikely to be conserved. Furthermore, we calculated the salt bridge between ACE2-RBD using a 4 Å cut-off distance. The native ACE2-RBD showed a total of 112 salt bridges over 10000 frames. In contrast, the mutants showed higher salt bridges, and omicron showed the highest number of salt bridges among the mutants (197 salt bridges). This indicates that the salt bridge formation between ACE2-RBD also plays a crucial role in the stabilization of binding.

ACE2-RBD binding energy

To gain further insight into the dissociation events between ACE2-RBD, we performed umbrella sampling simulations to calculate the potential of the mean force (PMF) for the complete dissociation of RBD from ACE2 (Figure S16). The wild complex showed a dissociation energy of 17.82 kcal/mol, while the omicron variant showed the highest binding energy at 25.10 kcal/mol. Molecular mechanics generalized Born surface area methods have been used in various studies to calculate the binding energy, but here, we did not consider the sampling of the relative rotational, diffusion, and conformational dynamics of RBDS and ACE2s. Our previous studies have reported the binding energies of native, single, double, and triple mutants, and identified critical residues using the alanine scanning method [20]. Here, we observed that conformational waves traveling from the mutant site to the binding site induced conformational changes and rearrangement of residues at the binding site, leading to higher residue interactions. It is crucial to understand ACE2

dynamics induced by RBD binding through long-term simulations. Therefore, we evaluated ACE2 dynamics in the native open and closed states using 10 µs of all-atom simulations.

Dynamics of Angiotensin-converting enzyme 2 and B38 neutralising antibody

The dynamics of the ACE2 receptor were evaluated from 10 µs all-atom simulations of five structures: apo open state (PDB ID:1R42), inhibitor-bound closed state (PDB ID:1R4L), complex state with the receptor-binding domain of a spike protein from SARS-CoV-1 (PDB ID:2AJF), complex state with the receptor-binding domain of a chimeric construct of SARS-CoV-2 (PDB ID: 6VW1), and complex state with the receptor-binding domain of a spike protein from SARS-CoV-2 (PDB ID:6M17) [36]. Here, we calculated the principal components to comprehend the conformational changes occurring in the ACE2 receptor throughout the 10 µs simulation (Figure 2). These motions allowed us to identify the principal structural features responsible for the changes induced by the RBD, as well as to determine highly flexible or rigid regions of the protein that contribute to these features. PCA can also be used to identify collective motions that occur in a protein, such as the opening or closing of a protein domain or the movement of a protein along a particular axis. Through the identification of these collective motions, a better understanding of the functional characteristics of the receptor and its interaction with the RBD can be achieved. The unbound state of the receptor exhibits a collective representation of the principal components in a 2D projection. Moreover, the 3D projection of the free energy landscape revealed stable receptor dynamics with global minima. In contrast, the closed conformation displayed increased fluctuations in the presence of local minima, eventually finding stable positions towards the end of the simulation. The PCA components revealed the distribution of eigenvectors across a wide range relative to the apo state. CoV1 and CoV2 (6VW1) exhibited multiple minima and high receptor fluctuations. Conversely, the 6M17 structure exhibited a global minimum with fewer

conformational transitions. Binding of RBD stabilizes the receptor earlier than the apo state, as shown by the free energy landscape. Furthermore, the distribution of RMS fluctuations revealed a stable distribution of backbone fluctuations, as illustrated by the violin plot of the RMSD. The binding of the COV2 receptor results in stabilization of the ACE2 receptor and possible fast signal transduction, which may lead to faster transmissibility. Additionally, clustering analysis of the ACE2 receptor revealed that the unbound protein exhibited a larger number of clusters (520) compared to the closed, CoV1, 6VW1, and 6M17 forms, which exhibited 192, 122, 126, and 56 independent diverse conformations, respectively(Figure 3). These results suggest that RBD binding restricts the conformational freedom of the receptor. Cluster analysis of the ACE2 apo form indicated significant structural heterogeneity with 530 distinct structural clusters. Conversely, the ACE2-RBD complex exhibited only 56 clusters, indicating a much greater degree of structural homogeneity. The higher number of clusters observed in the ACE2 apo form suggested that the protein was structurally more flexible in its unbound state. This flexibility may be important for the protein to undergo conformational changes upon binding with the RBD and to accommodate the RBD-binding interface. Furthermore, the structural heterogeneity observed in the ACE2 apo form may play a role in the promiscuity of viral entry, as it may allow the protein to interact with various related and unrelated ligands. However, the lower number of clusters observed in the ACE2-RBD complex suggests that the interaction is more structurally rigid and less flexible. This rigidity may be important for stabilizing the complex and ensuring proper orientation of the RBD-binding interface with ACE2. The greater structural homogeneity observed in the ACE2-RBD complex may also explain why neutralizing antibodies and vaccines are primarily directed towards the RBD-binding interface. Yan Wu et al. reported that human-origin monoclonal antibodies binding to the spike glycoprotein receptor binding domain of the virus can

reduce virus titers in infected lungs and lower infectivity in vivo mouse models [37]. Our findings suggest that the B38 antibody-bound RBD undergoes fewer structural transitions than the apo state, likely because of the strong binding of the antibody, which restricts the conformational dynamics of the RBD domain (Figure 4). This tight binding leads to reduced binding affinity with the ACE2 receptor, ultimately resulting in reduced transmissibility of the virus, as reported in experimental studies on mouse models, which show that the apo state exhibits multiple movements of residues, whereas antibody-bound RBD indicates confined movements. The free energy landscape of the antibody-bound RBD also suggests that the domain is at a deep global minimum during microsecond simulations, indicating the restricted movement of RBD residues (Figure 5). The clustering of backbone atoms further confirms that the apo state has a higher number of clusters than the antibody-bound state, indicating restricted movements of RBD residues; interestingly, the RBD interaction with ACE2 showed slower fluctuations compared to antibody-bound RBD binding. More clusters were also observed when the RBD-nAbs interacted, suggesting that the binding of neutralizing antibodies restricted RBD fluctuations, reduced transmissibility, and increased receptor movements, leading to higher structural flexibility (Figure S15 and S16). The free energy landscape with multiple local minima also indicated unstable receptor RBD interactions due to the strong binding of the B38 neutralizing antibody.

Conclusion

We presented the dynamics of ACE2-RBD using long-time all-atom molecular dynamics simulations. The structural stability and dynamics of the RBD of wild, alpha, alpha+, beta, gamma, delta, lambda, kappa, epsilon, and omicron with ACE2 receptors show induced conformational transitions from RBD to ACE2 receptor. Conformational changes arise from a single point mutation or multiple mutations in the RBD that determine binding affinity. Conformational waves

from the point mutation site travel through the RBD domain and reach the ACE2 receptor. These conformational waves changed the orientation of the RBD residue at the binding site. This results in higher hydrogen bond energy and stronger electrostatic interactions. Furthermore, the dynamics of ACE2 apo, open, closed, and RBD-bound revealed the induced transformation and structural stability of the ACE2 receptor. RBD binding restricts the conformational freedom of the receptors, which prevents the binding of the designated ligands. The ACE2 receptor shows significant structural heterogeneity, whereas it is binding to the RBD domain indicates a much greater degree of structural homogeneity. We found that the receptor is more flexible in its unbound state, and the binding of RBD domains changes it through induced structural transitions. The structural heterogeneity observed in the ACE2 unbound form plays a role in the promiscuity of viral entry as it may allow the protein to interact with various related and unrelated ligands. Furthermore, rigidity may be important for stabilizing the complex and ensuring the proper orientation of the RBD-binding interface with ACE2. The greater structural homogeneity observed in the ACE2-RBD complex revealed the effectiveness of neutralizing antibodies and vaccines that are primarily directed towards the RBD-binding interface. Finally, the binding of the B38 antibody revealed restricted conformational transitions in the RBD and ACE2 receptors due to the tight binding of the monoclonal neutralizing antibody.

Supporting Information

Supporting Information provides additional figures and tables.

Acknowledgment

Author thank to RIKEN R-CCS Supercomputer Fugaku for the simulations through project hp210295.

Reference

1 R. Lu, X. Zhao, J. Li, P. Niu, B. Yang, H. Wu, W. Wang, H. Song, B. Huang, N. Zhu, Y. Bi, X. Ma, F. Zhan, L. Wang, T. Hu, H. Zhou, Z. Hu, W. Zhou, L. Zhao, J. Chen, Y. Meng, J. Wang, Y. Lin, J. Yuan, Z. Xie, J. Ma, W. J. Liu, D. Wang, W. Xu, E. C. Holmes, G. F. Gao, G. Wu, W. Chen, W. Shi and W. Tan, Genomic characterisation and epidemiology of 2019 novel coronavirus: implications for virus origins and receptor binding, *Lancet*, 2020, **395**, 565–574.

2 M. W. Zhuang, Y. Cheng, J. Zhang, X. M. Jiang, L. Wang, J. Deng and P. H. Wang, Increasing host cellular receptor—angiotensin-converting enzyme 2 expression by coronavirus may facilitate 2019-nCoV (or SARS-CoV-2) infection, *J. Med. Virol.*, 2020, **92**, 2693–2701.

3 W. Ni, X. Yang, D. Yang, J. Bao, R. Li, Y. Xiao, C. Hou and H. Wang, Role of angiotensin-converting enzyme 2 (ACE2) in COVID-19, 2020, 1–10.

4 W. Tai, L. He, X. Zhang, J. Pu, D. Voronin, S. Jiang, Y. Zhou and L. Du, Characterization of the receptor-binding domain (RBD) of 2019 novel coronavirus: implication for development of RBD protein as a viral attachment inhibitor and vaccine, *Cell. Mol. Immunol.*, 2020, **17**, 613–620.

5 K. Ramanathan, D. Antognini, A. Combes, M. Paden, B. Zakhary, M. Ogino, G. Maclaren and D. Brodie, Clinical features of patients infected with 2019 novel coronavirus in Wuhan, China, *Lancet*, 2020, **395**, 497–506.

6 D. Paraskevis, E. G. Kostaki, G. Magiorkinis, G. Panayiotakopoulos, G. Sourvinos and S. Tsiodras, Full-genome evolutionary analysis of the novel corona virus (2019-nCoV)

rejects the hypothesis of emergence as a result of a recent recombination event, *Infect. Genet. Evol.*, 2020, **79**, 104212.

7 N. Zhu, D. Zhang, W. Wang, X. Li, B. Yang, J. Song, X. Zhao, B. Huang, W. Shi, R. Lu, P. Niu, F. Zhan, X. Ma, D. Wang, W. Xu, G. Wu, G. F. Gao and W. Tan, A Novel Coronavirus from Patients with Pneumonia in China, 2019, *N. Engl. J. Med.*, 2020, **382**, 727–733.

8 C. K. Wibmer, F. Ayres, T. Hermanus, M. Madzivhandila, P. Kgagudi, B. Oosthuysen, B. E. Lambson, T. de Oliveira, M. Vermeulen, K. van der Berg, T. Rossouw, M. Boswell, V. Ueckermann, S. Meiring, A. von Gottberg, C. Cohen, L. Morris, J. N. Bhiman and P. L. Moore, SARS-CoV-2 501Y.V2 escapes neutralization by South African COVID-19 donor plasma, *Nat. Med.*, 2021, **27**, 622–625.

9 S. A. Madhi, V. Baillie, C. L. Cutland, M. Voysey, A. L. Koen, L. Fairlie, S. D. Padayachee, K. Dheda, S. L. Barnabas, Q. E. Bhorat, C. Briner, G. Kwatra, K. Ahmed, P. Aley, S. Bhikha, J. N. Bhiman, A. E. Bhorat, J. du Plessis, A. Esmail, M. Groenewald, E. Horne, S.-H. Hwa, A. Jose, T. Lambe, M. Laubscher, M. Malahleha, M. Masenya, M. Masilela, S. McKenzie, K. Molapo, A. Moultrie, S. Oelofse, F. Patel, S. Pillay, S. Rhead, H. Rodel, L. Rossouw, C. Taoushanis, H. Tegally, A. Thombrayil, S. van Eck, C. K. Wibmer, N. M. Durham, E. J. Kelly, T. L. Villafana, S. Gilbert, A. J. Pollard, T. de Oliveira, P. L. Moore, A. Sigal and A. Izu, Efficacy of the ChAdOx1 nCoV-19 Covid-19 Vaccine against the B.1.351 Variant, *N. Engl. J. Med.*, 2021, **384**, 1885–1898.

10 C. H. S. da Costa, C. A. B. de Freitas, C. N. Alves and J. Lameira, Assessment of mutations on RBD in the Spike protein of SARS-CoV-2 Alpha, Delta and Omicron variants, *Sci. Rep.*, 2022, **12**, 1–10.

11 A. Khan, T. Zia, M. Suleman, T. Khan, S. S. Ali, A. A. Abbasi, A. Mohammad and D. Q. Wei, Higher infectivity of the SARS-CoV-2 new variants is associated with K417N/T, E484K, and N501Y mutants: An insight from structural data, *J. Cell. Physiol.*, 2021, **236**, 7045–7057.

12 J. Zahradník, S. Marciano, M. Shemesh, E. Zoler, D. Harari, J. Chiaravalli, B. Meyer, Y. Rudich, C. Li, I. Marton, O. Dym, N. Elad, M. G. Lewis, H. Andersen, M. Gagne, R. A. Seder, D. C. Douek and G. Schreiber, SARS-CoV-2 variant prediction and antiviral drug design are enabled by RBD in vitro evolution, *Nat. Microbiol.*, 2021, **6**, 1188–1198.

13 S. Ozono, Y. Zhang, H. Ode, K. Sano, T. S. Tan, K. Imai, K. Miyoshi, S. Kishigami, T. Ueno, Y. Iwatani, T. Suzuki and K. Tokunaga, SARS-CoV-2 D614G spike mutation increases entry efficiency with enhanced ACE2-binding affinity, *Nat. Commun.*, , DOI:10.1038/s41467-021-21118-2.

14 S. K. Saxena, S. Kumar, S. Ansari, J. T. Paweska, V. K. Maurya, A. K. Tripathi and A. S. Abdel-Moneim, Characterization of the novel SARS-CoV-2 Omicron (B. 1.1. 529) variant of concern and its global perspective, *J. Med. Virol.*, 2022, **94**, 1738–1744.

15 L. Zhou, L. Wu, C. Peng, Y. Yang, Y. Shi, L. Gong, Z. Xu and W. Zhu, Predicting spike protein NTD mutations of SARS-CoV-2 causing immune evasion by molecular dynamics simulations, *Phys. Chem. Chem. Phys.*, 2022, **24**, 3410–3419.

16 D. Xiong, X. Zhao, S. Luo and L. Duan, Insights from computational analysis: how does the SARS-CoV-2 Delta (B. 1.617. 2) variant hijack ACE2 more effectively?, *Phys. Chem. Chem. Phys.*, 2022, **24**, 8683–8694.

17 W. R. Strohl, Z. Ku, Z. An, S. F. Carroll, B. A. Keyt and L. M. Strohl, *Passive Immunotherapy Against SARS-CoV-2: From Plasma-Based Therapy to Single Potent Antibodies in the Race to Stay Ahead of the Variants*, Springer International Publishing, 2022, vol. 36.

18 N. Maroli, B. Bhasuran, J. Natarajan and P. Kolandaivel, The potential role of procyanidin as a therapeutic agent against SARS-CoV-2: a text mining, molecular docking and molecular dynamics simulation approach, *J. Biomol. Struct. Dyn.*, 2022, **40**, 1230–1245.

19 F. Wu, S. Zhao, B. Yu, Y. M. Chen, W. Wang, Z. G. Song, Y. Hu, Z. W. Tao, J. H. Tian, Y. Y. Pei, M. L. Yuan, Y. L. Zhang, F. H. Dai, Y. Liu, Q. M. Wang, J. J. Zheng, L. Xu, E. C. Holmes and Y. Z. Zhang, A new coronavirus associated with human respiratory disease in China, *Nature*, 2020, **579**, 265–269.

20 A. Aggarwal, S. Naskar, N. Maroli, B. Gorai, N. M. Dixit and P. K. Maiti, Mechanistic insights into the effects of key mutations on SARS-CoV-2 RBD-ACE2 binding, *Phys. Chem. Chem. Phys.*, 2021, **23**, 26451–26458.

21 A. Deshpande, B. D. Harris, L. Martinez-Sobrido, J. J. Kobie and M. R. Walter, Epitope Classification and RBD Binding Properties of Neutralizing Antibodies Against SARS-CoV-2 Variants of Concern, *Front. Immunol.*, 2021, **12**, 1–14.

22 W. Yin, Y. Xu, P. Xu, X. Cao, C. Wu, C. Gu, X. He, X. Wang, S. Huang, Q. Yuan and others, Structures of the Omicron spike trimer with ACE2 and an anti-Omicron antibody, *Science (80-.).*, 2022, **375**, 1048–1053.

23 R. Yan, Y. Zhang, Y. Li, L. Xia, Y. Guo and Q. Zhou, Structural basis for the recognition of SARS-CoV-2 by full-length human ACE2, *Science (80-.).*, 2020, **367**, 1444–1448.

24 E. F. Pettersen, T. D. Goddard, C. C. Huang, G. S. Couch, D. M. Greenblatt, E. C. Meng and T. E. Ferrin, UCSF Chimera - A visualization system for exploratory research and analysis, *J. Comput. Chem.*, 2004, **25**, 1605–1612.

25 J. Huang and A. D. MacKerell Jr, CHARMM36 all-atom additive protein force field: Validation based on comparison to NMR data, *J. Comput. Chem.*, 2013, **34**, 2135–2145.P. Mark and L. Nilsson, Structure and dynamics of the TIP3P, SPC, and SPC/E water models at 298 K, *J. Phys. Chem. A*, 2001, **105**, 9954–9960.

26 U. Essmann, L. Perera, M. L. Berkowitz, T. Darden, H. Lee and L. G. Pedersen, A smooth particle mesh Ewald method, *J. Chem. Phys.*, 1995, **103**, 8577–8593.

27 B. Hess, H. Bekker, H. J. C. Berendsen and J. G. E. M. Fraaije, LINCS: A Linear Constraint Solver for molecular simulations, *J. Comput. Chem.*, 1997, **18**, 1463–1472.

28 B. Hess, C. Kutzner, D. Van Der Spoel and E. Lindahl, GRGMACS 4: Algorithms for highly efficient, load-balanced, and scalable molecular simulation, *J. Chem. Theory Comput.*, 2008, **4**, 435–447.

29 S. Kumar, D. Bouzida, R. H. Swendsen, P. A. Kollman and J. M. Rosenberg, The weighted histogram analysis method for free-energy calculations on biomolecules, *J. Comput. Chem.*, 1992, **13**, 1011–1021.

30 S. P. Lloyd, Least Squares Quantization in PCM, *IEEE Trans. Inf. Theory*, 1982, **28**, 129–137.

31 S. Uw, Spectral Clustering, *Encycl. Mach. Learn. Data Min.*, 2017, 1167–1167.

32 Y. Wang, M. Liu and J. Gao, Enhanced receptor binding of SARS-CoV-2 through networks of hydrogen-bonding and hydrophobic interactions, *Proc. Natl. Acad. Sci.*, 2020, **117**, 13967–13974.

33 J. M. Delgado, N. Duro, D. M. Rogers, A. Tkatchenko, S. A. Pandit and S. Varma, Molecular basis for higher affinity of SARS-CoV-2 spike RBD for human ACE2 receptor, *Proteins Struct. Funct. Bioinforma.*, 2021, **89**, 1134–1144.

34 Y. Watanabe, J. D. Allen, D. Wrapp, J. S. McLellan and M. Crispin, Site-specific glycan analysis of the SARS-CoV-2 spike, *Science (80-.).*, 2020, **369**, 330–333.

35 D. E. Shaw Research, "Molecular Dynamics Simulations Related to SARS-CoV-2," D. E. Shaw Research Technical Data, 2020. https://www.deshawresearch.com/downloads/download_trajectory_sarscov2.cgi/

36 Y. Wu, F. Wang, C. Shen, W. Peng, D. Li, C. Zhao, Z. Li, S. Li, Y. Bi, Y. Yang, Y. Gong, H. Xiao, Z. Fan, S. Tan, G. Wu, W. Tan, X. Lu, C. Fan, Q. Wang, Y. Liu, C. Zhang, J. Qi, G. F. Gao, F. Gao and L. Liu, A noncompeting pair of human neutralizing antibodies block COVID-19 virus binding to its receptor ACE2, *Science (80-.).*, 2020, **368**, 1274–1278.

Figures

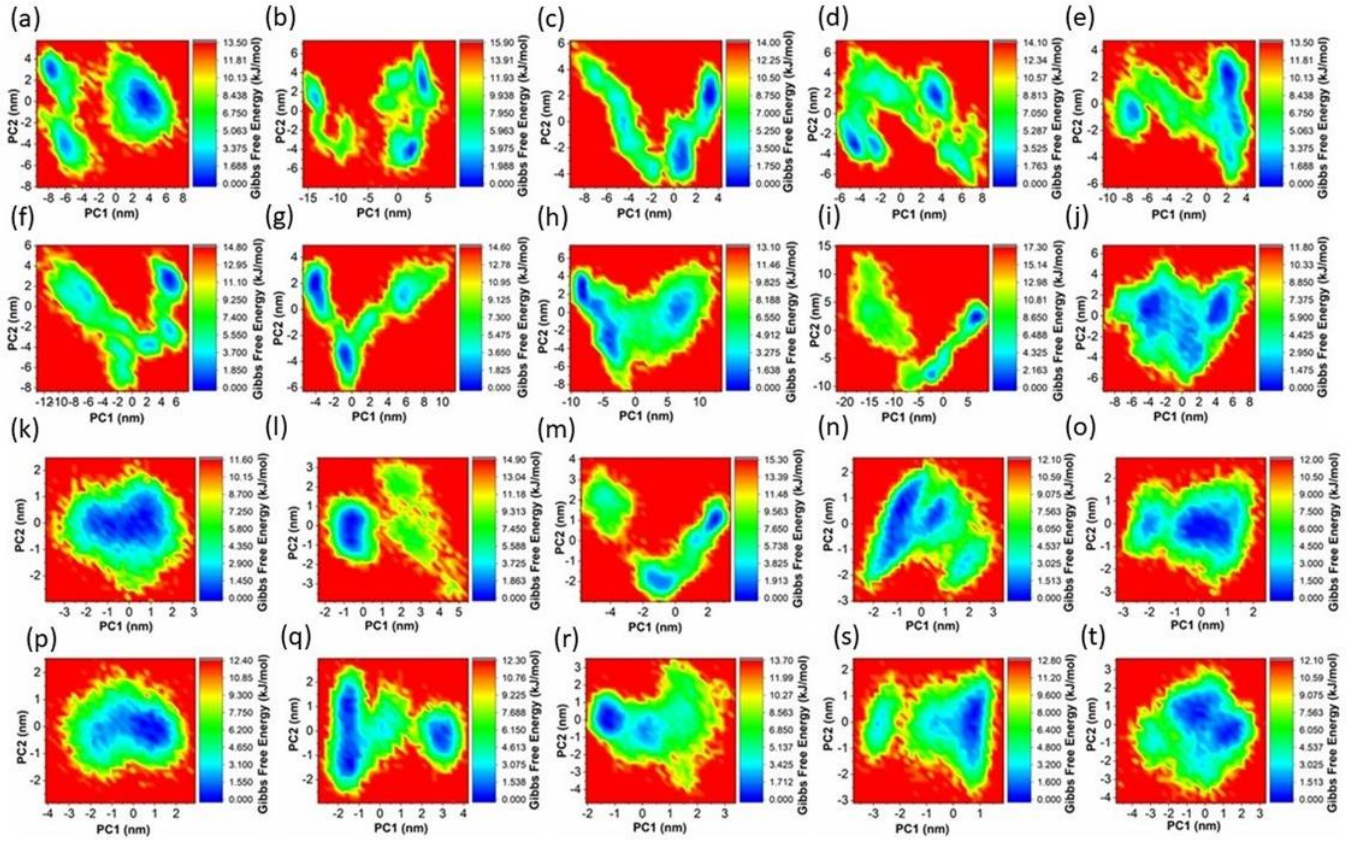

Figure 1. 2D-free energy landscape (FEL) constructed from first and second principal components a-j represent ACE2 receptor and k-t represent RBD. (a)wild,(b)alpha,(c)alpha+,(d)beta,(e)gamma,(f)delta,(g)epsilon,(h)kappa,(i)lambda, and (j)omicron. (k)wild,(l)alpha,(m)alpha+,(n)beta,(o)gamma,(p)delta,(q)epsilon,(r)kappa,(s)lambda, and (t)omicron. The wild ACE2 receptor shows deep and wide global minima along with well-connected local minima. Whereas the interaction with mutant RBD led to several deep local minima and omicron mutant shows global minima with multiple wells. This indicates the strong affinity of the RBD omicron variant with the ACE2 receptor. The interaction of this variant led the ACE2 to form global minima. In RBD, the wild shows global wide minima and among the variant, the stability increases when the number of mutations increases and the maximum is identified in the case of omicron mutant.

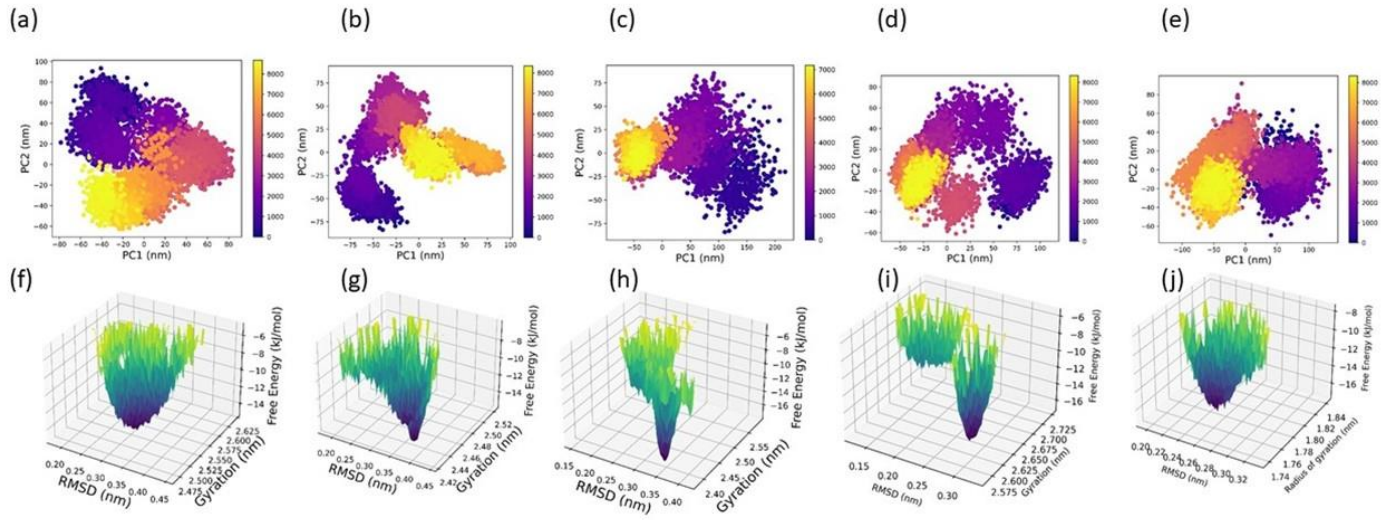

Figure 2. The distribution of principal components of ACE2 receptor and Free energy landscape. (a) apo, (b)closed ,(c)cov1, (d)6vw1, (e)6m17 represents the 2d representation of principal components. (f) apo, (g) closed,(h) cov1, (i) 6vw1, (j) 6m17 represents the 3-D free energy landscape obtained from RMSD of backbone atoms and radius of gyrations. The apo state had an ordered and centered distribution of clusters in the PCA plot, whereas the closed state was centered and showed an uneven distribution. The cov1 showed an expanded distribution of clusters that extended beyond the ranges observed in the apo and closed structures. The cov2 structure possesses evenly distributed clusters but isolated and tightly clustered regions. The apo structure distribution of the points is ordered and oriented towards the center, which also suggests a high degree of correlation between the different principal components. The difference in the clusters also indicates that the conformations may interact with different ligands or molecules in different ways. The closed state indicates that the receptor underwent significant conformational changes, resulting in reduced stability. The binding of RBD domains leads to higher flexibility and structural dynamics of the receptor. The apo state shows a wide distribution of FEL with a single well, indicating a conformational space and relatively low stability

in terms of ligand binding and receptor action. The closed state shows a wide distribution, but sharp and well represents a significant transition to a stable conformation. As expected, the ligand-bound receptor was more stable than the unbound apo state. The cov1 bound structure shows a wide distribution, but some parts have gone deep well, indicating that the receptor undergoes a significant conformational change. The cov2 bound state (6vw1) showed multiple stable conformations with different levels of stability, whereas 6m17 showed a deep well with the possible receptor conformational space.

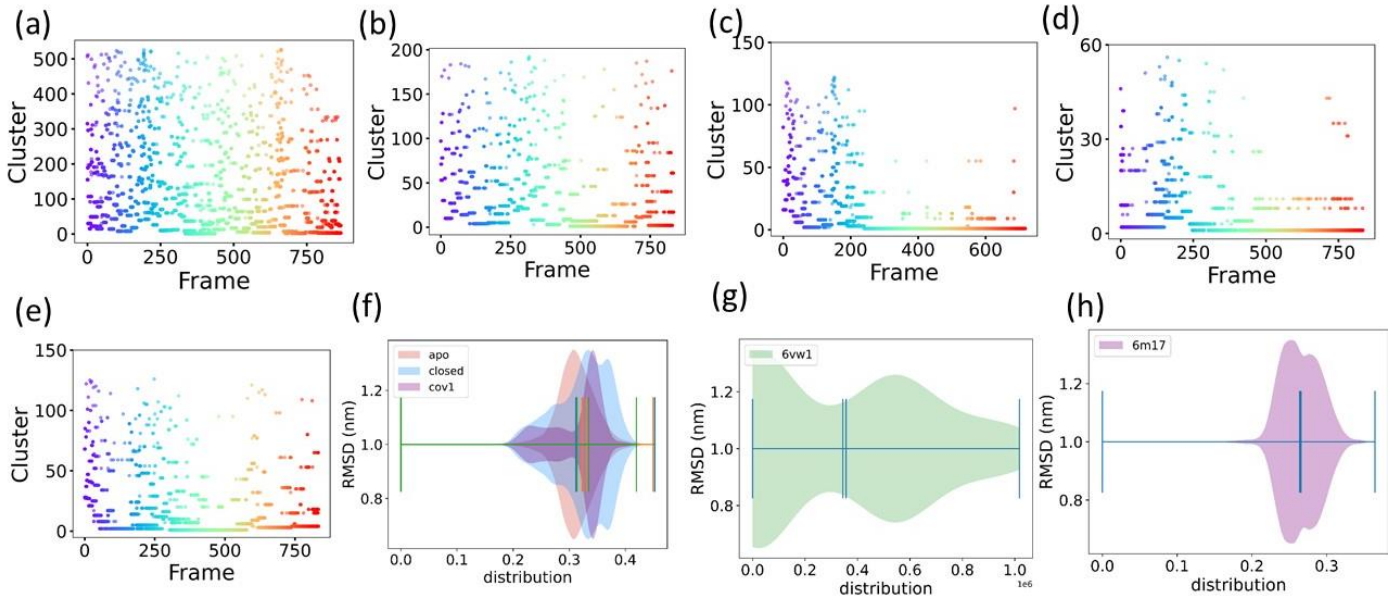

Figure 3. The clustering of ACE2 receptor (a) apo, (b) closed, (c) cov1, (d) 6vw1, (e)6m17 with corresponding backbone RMSD distribution. A higher number of clusters in the ACE2 apo structure indicated conformational diversity and structural state. This indicates that the unbound apo state of the receptor has a greater number of conformational states. The binding of the inhibitor and RBD domains reduced the conformational spaces due to strong binding. The higher conformational flexibility of the

receptor help for the likelihood of interaction and leads to potential binding to different viral strains or mutants, which improve the transmissibility.

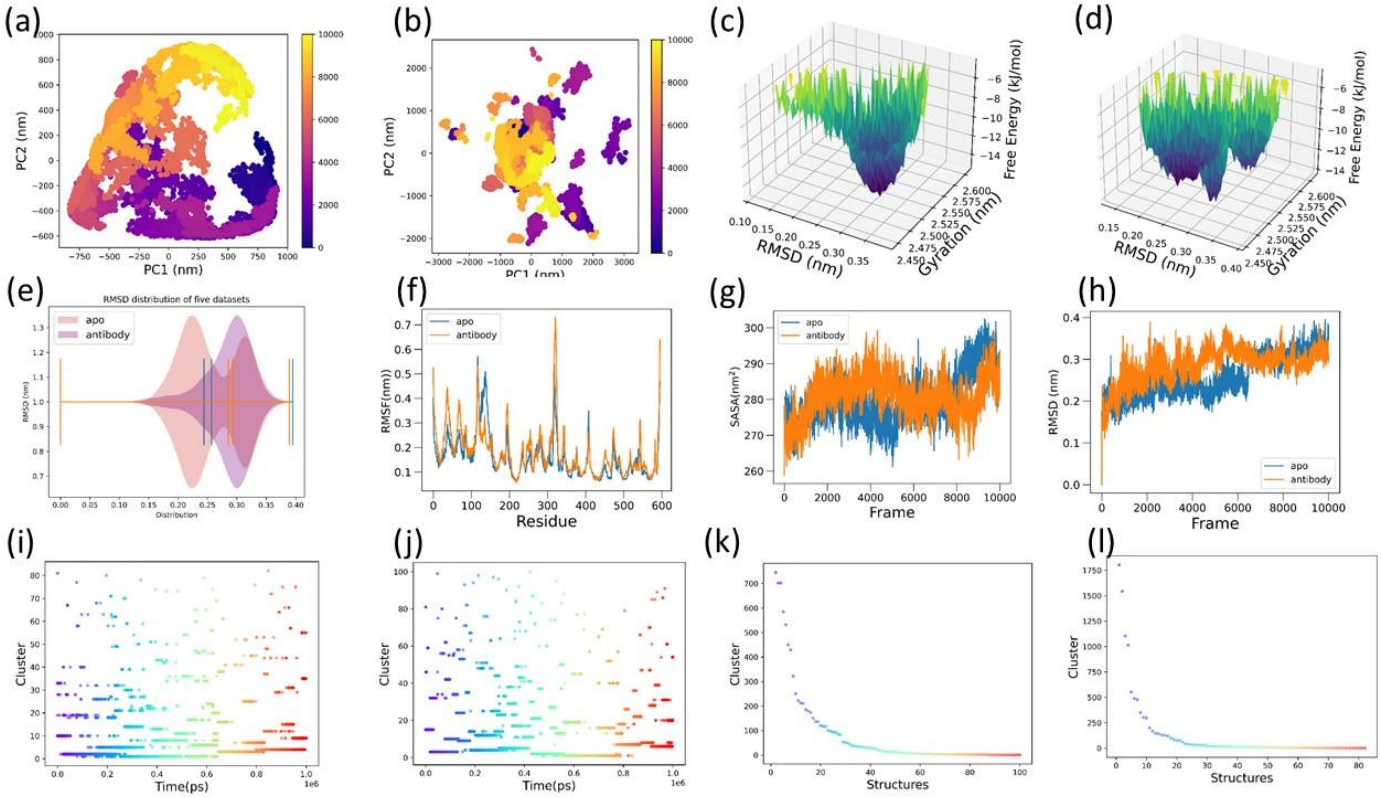

Figure 4. Dynamics of ACE2 receptor that bound with antibody inhibited RBD. (a) and (b) shows the PCs distribution of ACE2 receptor apo and RBD bound. The corresponding FEL generated from RMSD and radius of gyration is given in (c) and (d). The changes in RMS deviations and fluctuations are shown in (e), (f) and (h). (i) to (l) represent the clusters in each time frame and the cluster per structure. The wide distribution of PCs components indicates a broader range of conformational states in the apo state, whereas ACE2, which binds to the RBD that is inhibited by the B38 antibody, suggests

new conformational states and restricted certain motions that exist in the apo state of ACE2. This suggested that the antibody and its impact on the conformational dynamics of the ACE2-RBD complex. Antibody binding stabilizes or changes the binding regions of RBD and reduces the normal binding pattern with the ACE2 receptor. Furthermore, the FEL also suggested a stable and wide ACE2 conformation, which was restricted by the RBD by introducing multiple local minima states. In addition, the binding of RBD was found to alter the clusters and transformations of backbone atoms.

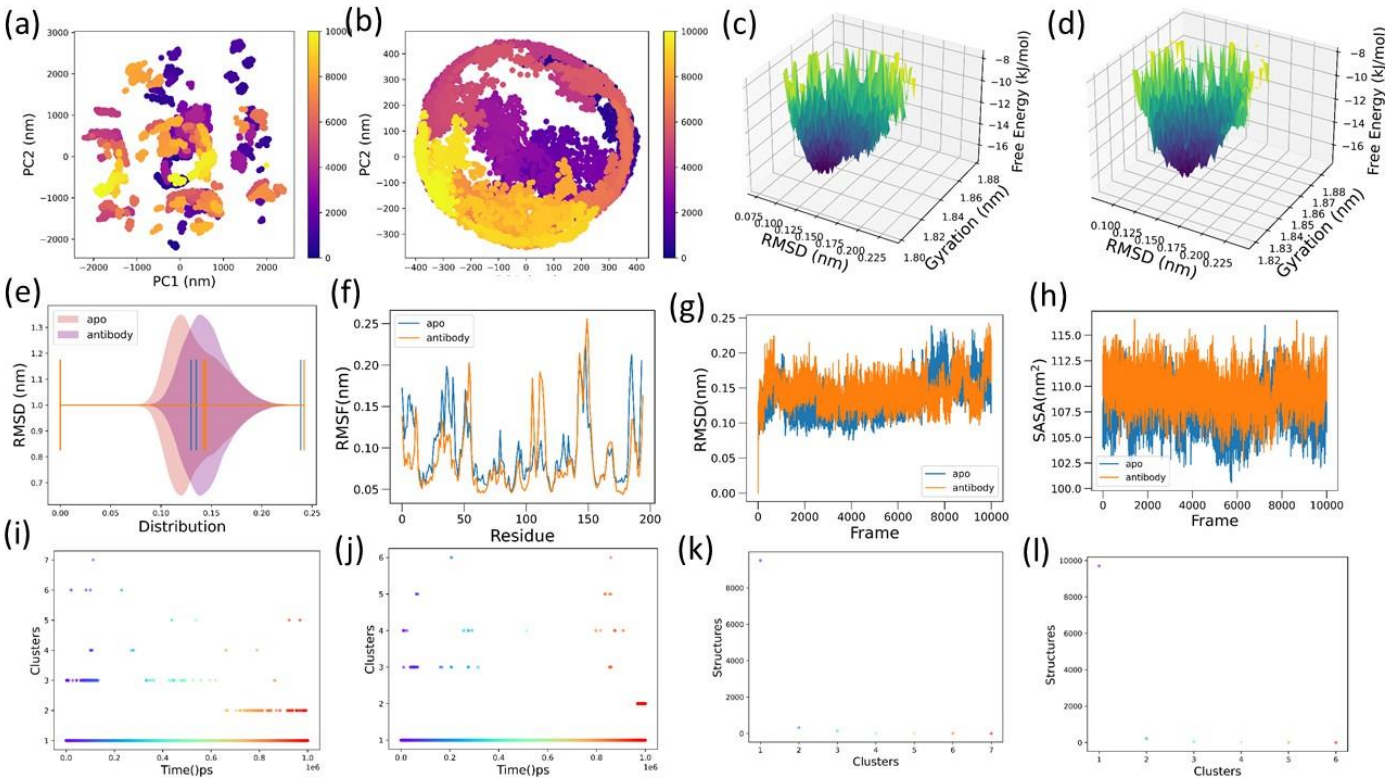

Figure 5. RBD dynamics with neutralizing antibody and ACE2 receptor. (a) The PC's representation of RBD that bound with neutralizing antibody. (b) PCs representation of RBD with ACE2 receptor which is inhibited by neutralizing antibody. (c) and (d) represents the corresponding free energy landscape obtained from RMSD and the radius of gyration. RMS distribution (e), RMSF (f) RMSD (g) and solvent accessible surface area (h) of RBD that bound with antibody. (i) to (l) represents the cluster per time and cluster per the structure of RBD.

Supporting Information

Riding the Wave: Unveiling the Conformational Waves from RBD to ACE2

Nikhil Maroli

Computational Biology Division, DRDO Center for Life Science, Bharathiar University Campus, Coimbatore 641046, Tamil Nadu, India

Corresponding author: scinikhil@gmail.com

Supporting Information

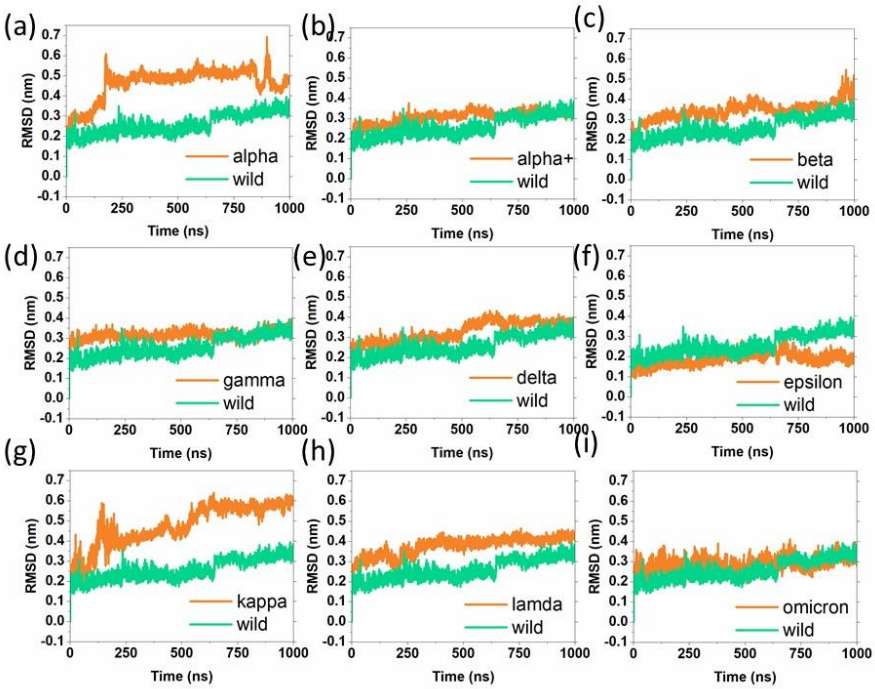

Figure S1. The root mean square deviations (RMSD) of ACE2 receptor backbone atoms when it bound with RBD mutant (a) alpha,(b)alpha+,(c)beta,(d)gamma,(e)delta,(f)epsilon,(g)kappa,(h)lambda, and (i) omicron.

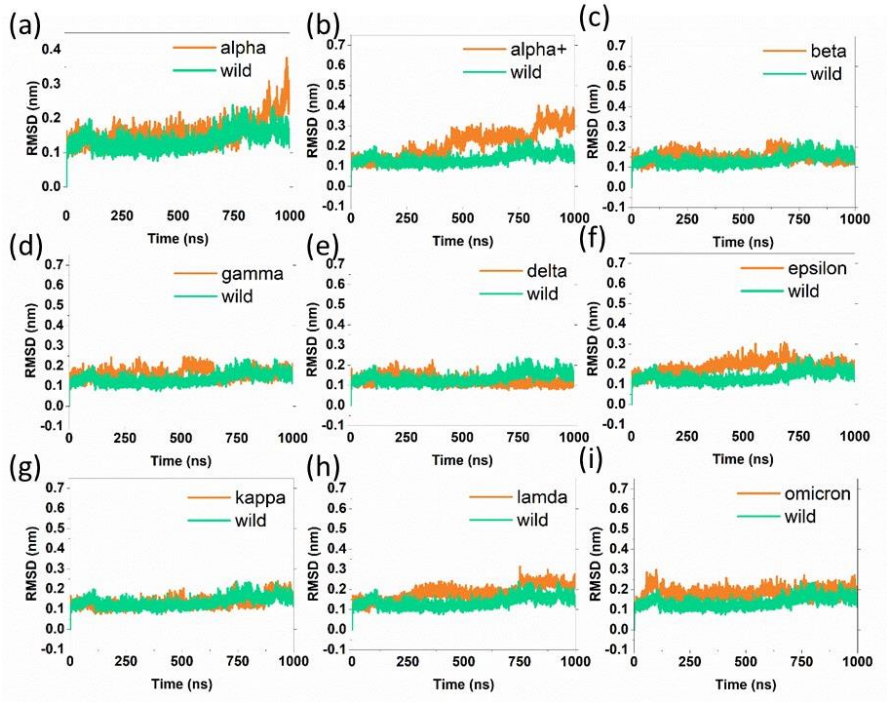

Figure S2. The root mean square deviations (RMSD) of RBD backbone atoms when they bound with ACE2 receptor (a) alpha,(b)alpha+,(c)beta,(d)gamma,(e)delta,(f)epsilon,(g)kappa,(h)lambda, and (i) omicron.

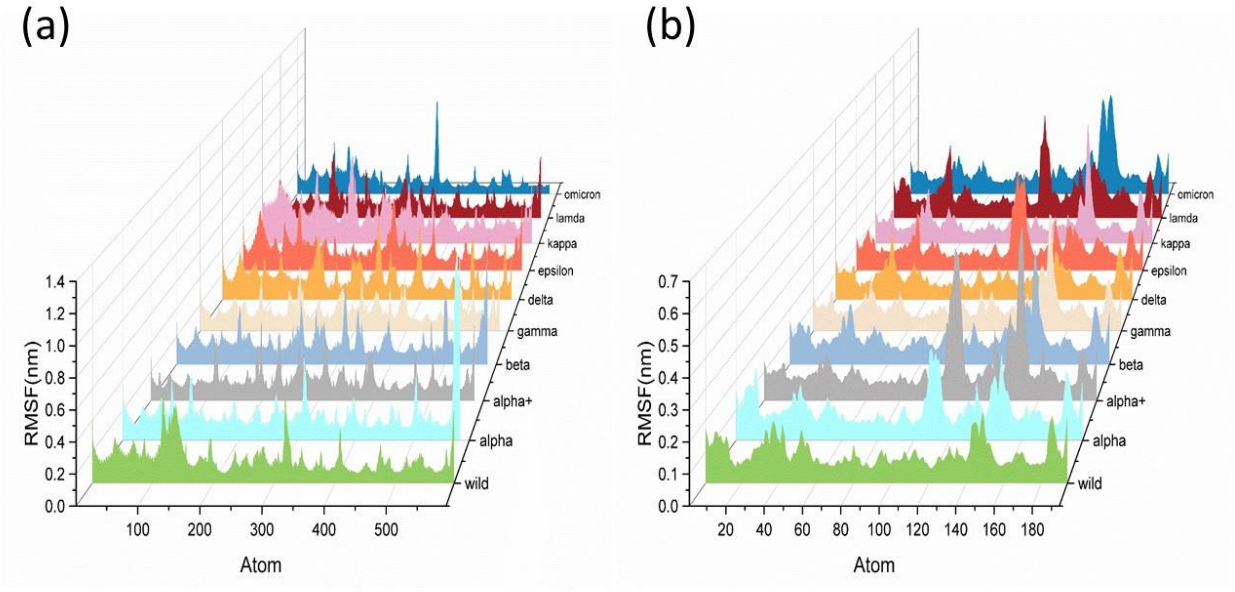

Figure S3. The root mean square fluctuations (RMSF) of (a) ACE2 receptor and (b) RBD wild and mutants.

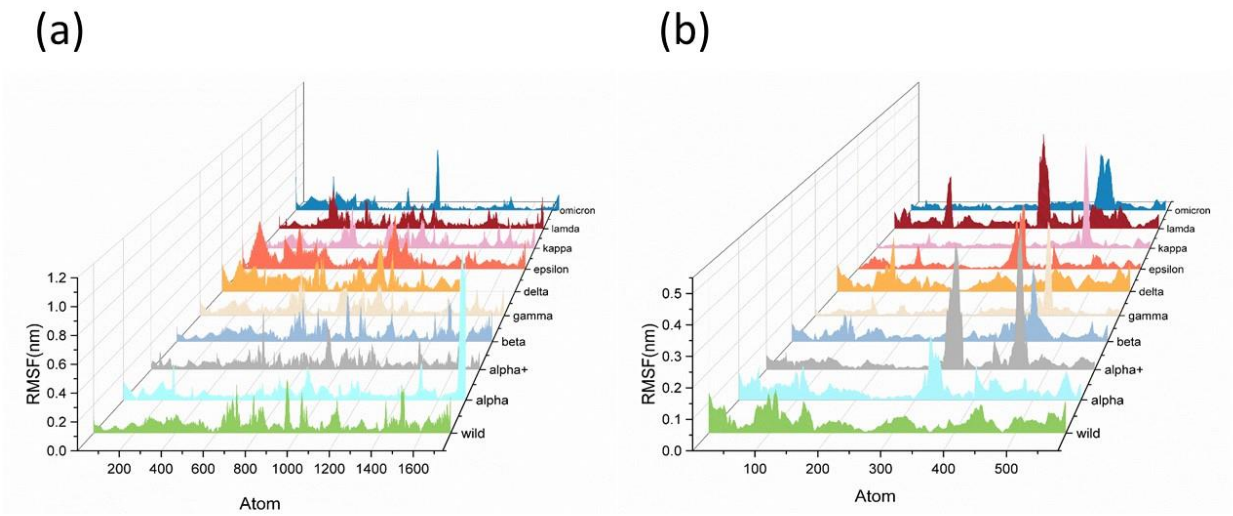

Figure S4. The root mean square fluctuations of backbone atoms obtained from PCA (a) ACE2 receptor and (b) RBD wild and mutants.

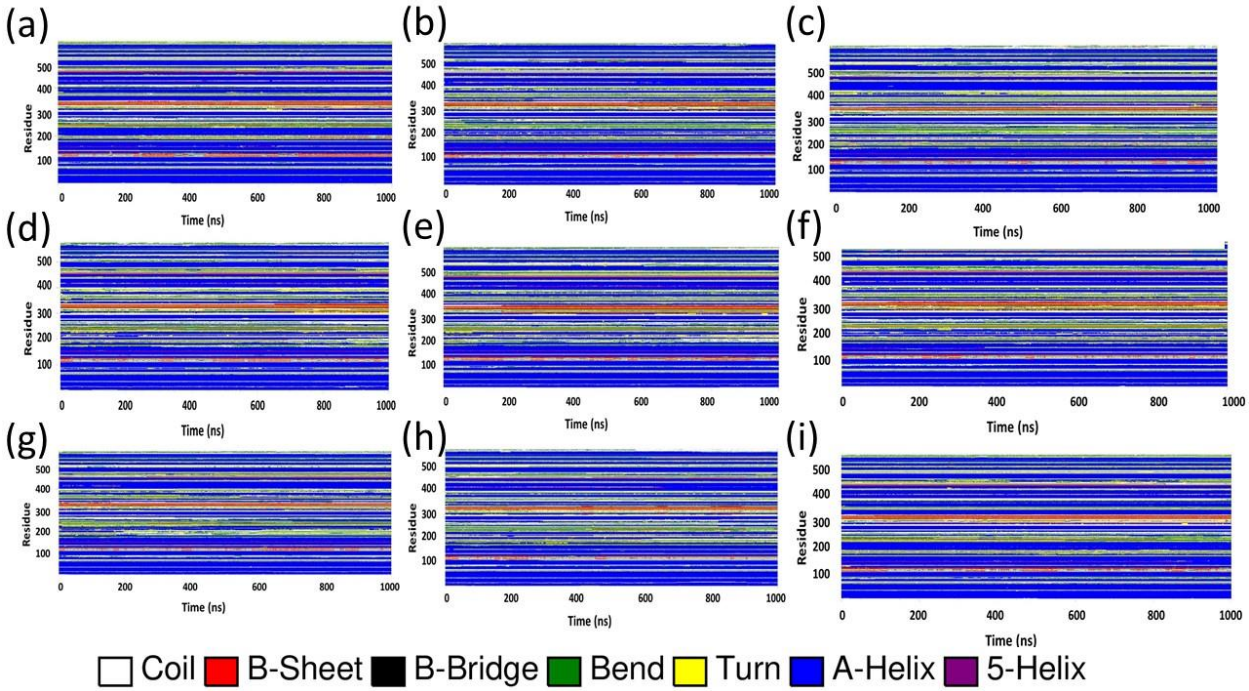

Figure S5. Time-dependent secondary structural changes of the ACE2 receptor. (a) wild,(b)alpha,(c)beta,(d)gamma,(e)delta,(f)epsilon,(g)kappa,(h)lambda, and (i) omicron.

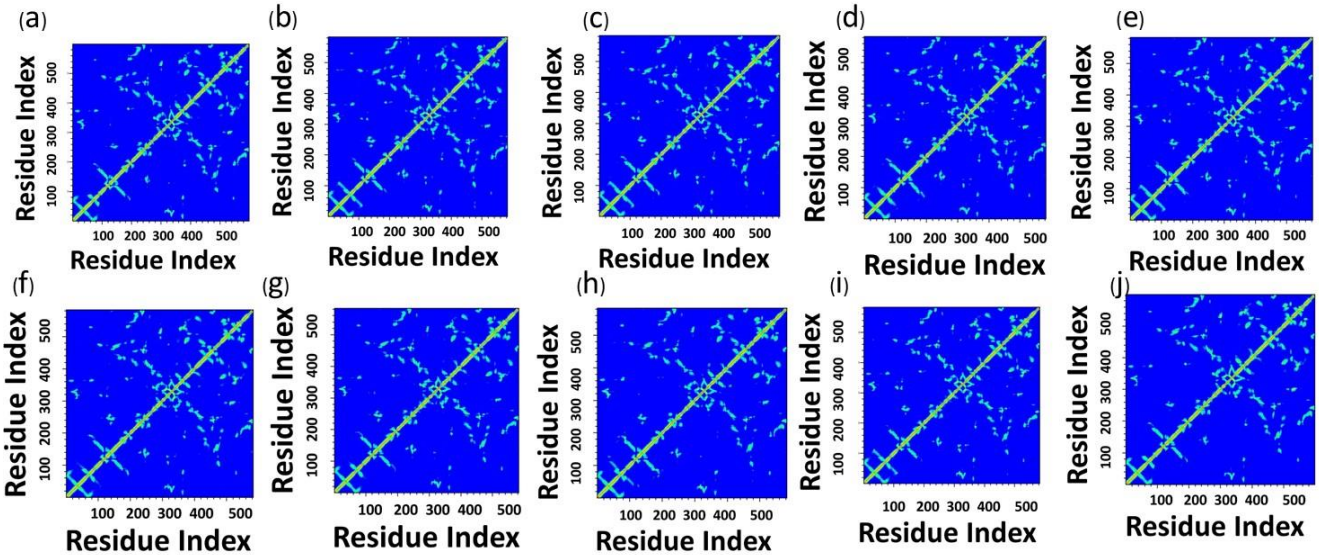

Figure S6. The residue-residue distance matrix was constructed for the ACE2 receptor. (a) Wild, (b) alpha, (c) alpha+, (d) beta, ,(e)gamma,(f)delta,(g)epsilon,(h)kappa,(i)lambda, and (j) omicron.

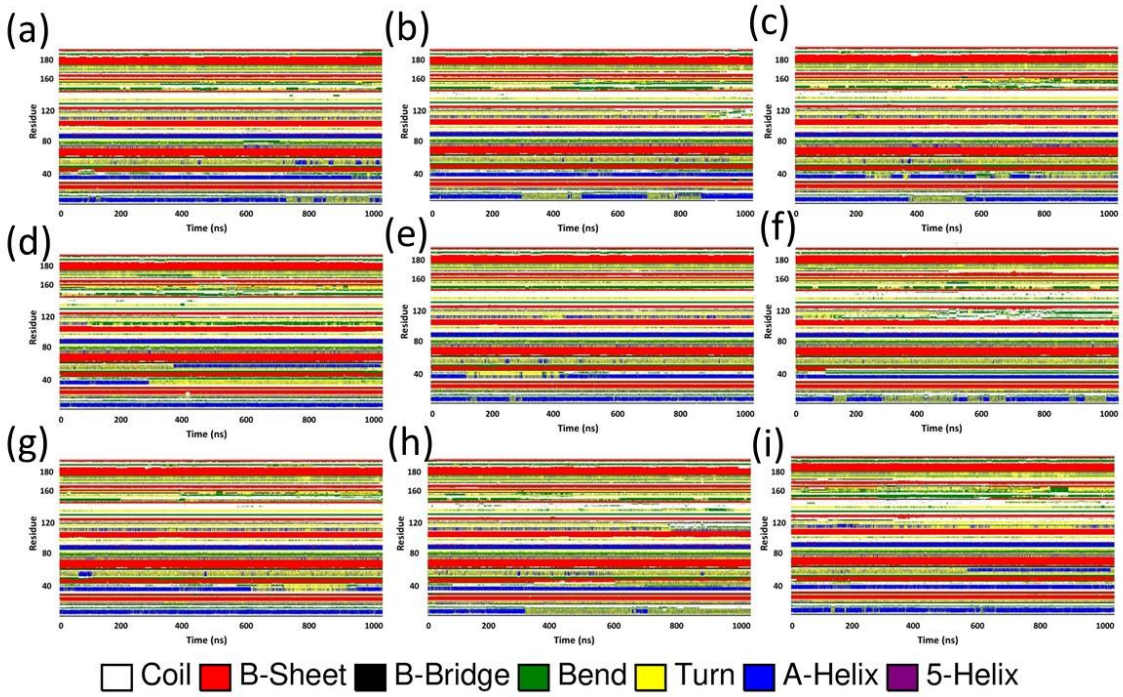

Figure S7. Time-dependent secondary structural changes of the RBD. (a) wild,(b)alpha,(c)beta,(d)gamma,(e)delta,(f)epsilon,(g)kappa,(h)lambda, and (i) omicron.

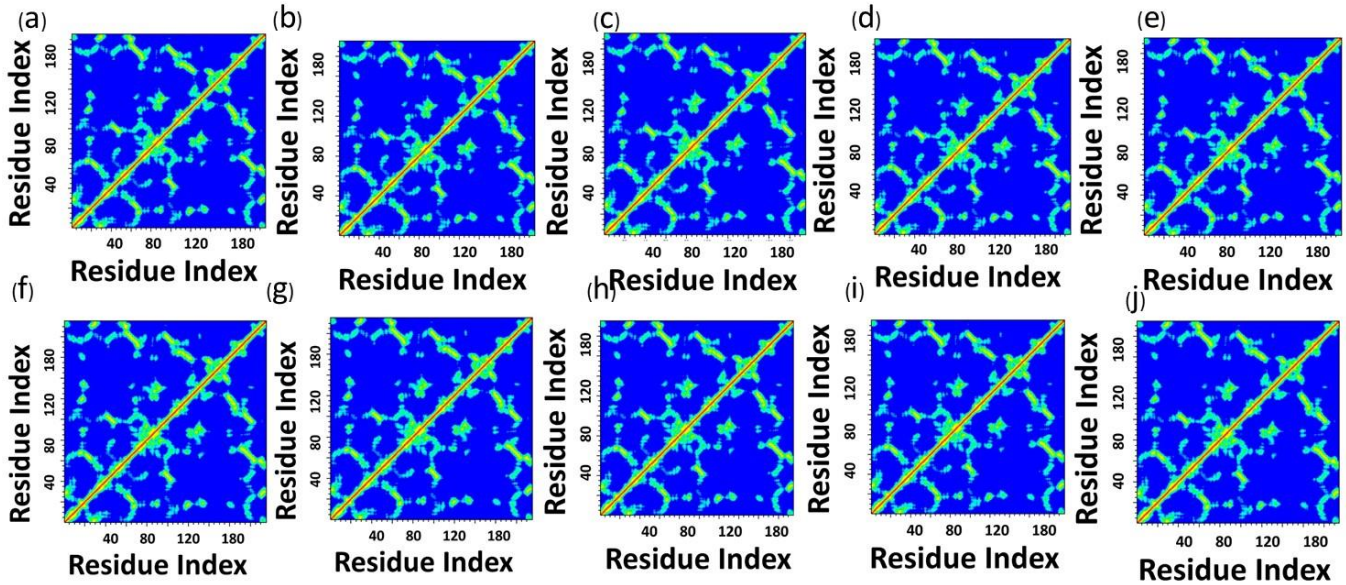

Figure S8. The residue-residue distance matrix was constructed for RBD. (a) Wild, (b) alpha, (c) alpha+, (d) beta, ,(e)gamma,(f)delta,(g)epsilon,(h)kappa,(i)lambda, and (j) omicron.

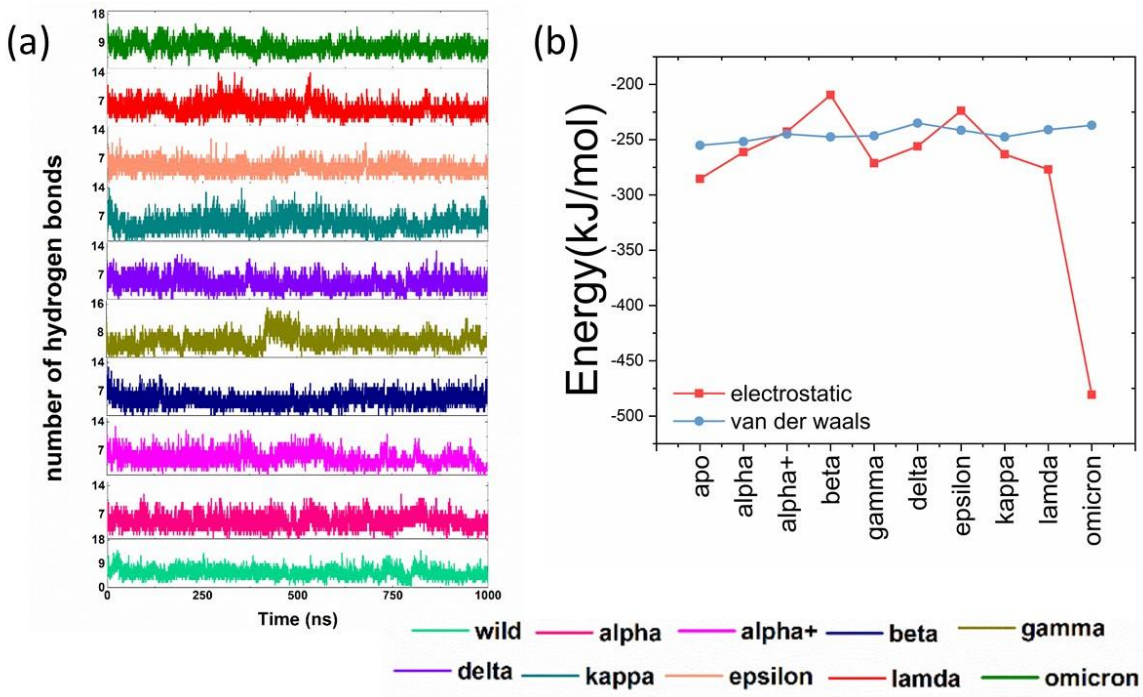

Figure S9. The number of hydrogen bonds formed between ACE2-RBD and mutants (a) and the average electrostatic and van der Waals interaction energy between ACE2-RBD mutants.

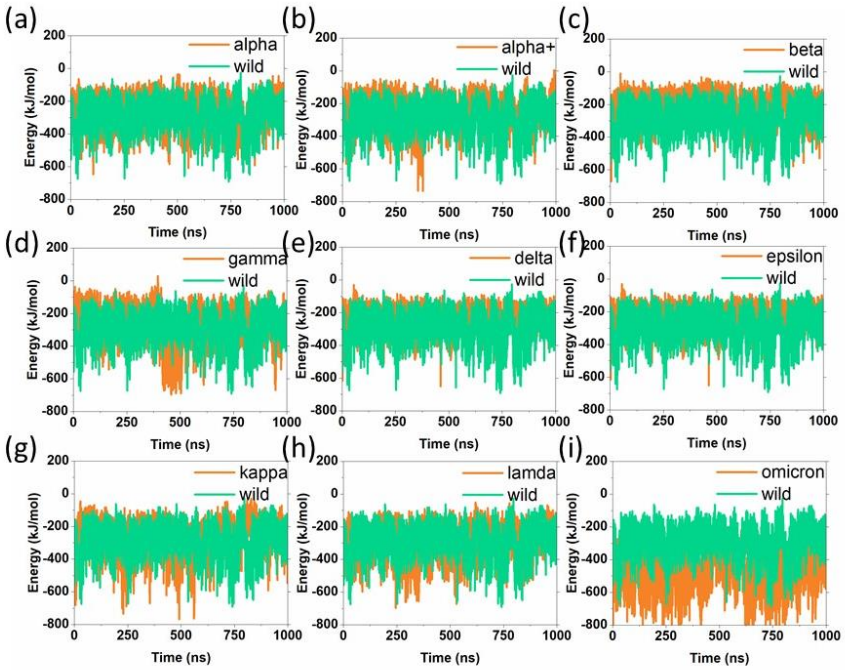

Figure S10. The electrostatic interaction energy over time between ACE2-RBD and mutants.

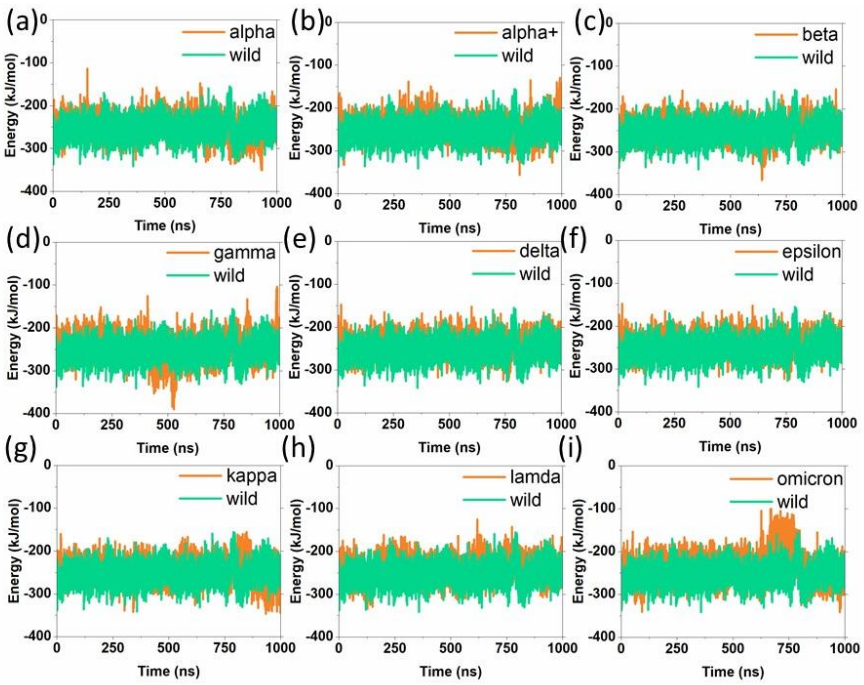

Figure S11. The van der Waals interaction energy over time between ACE2-RBD and mutants.

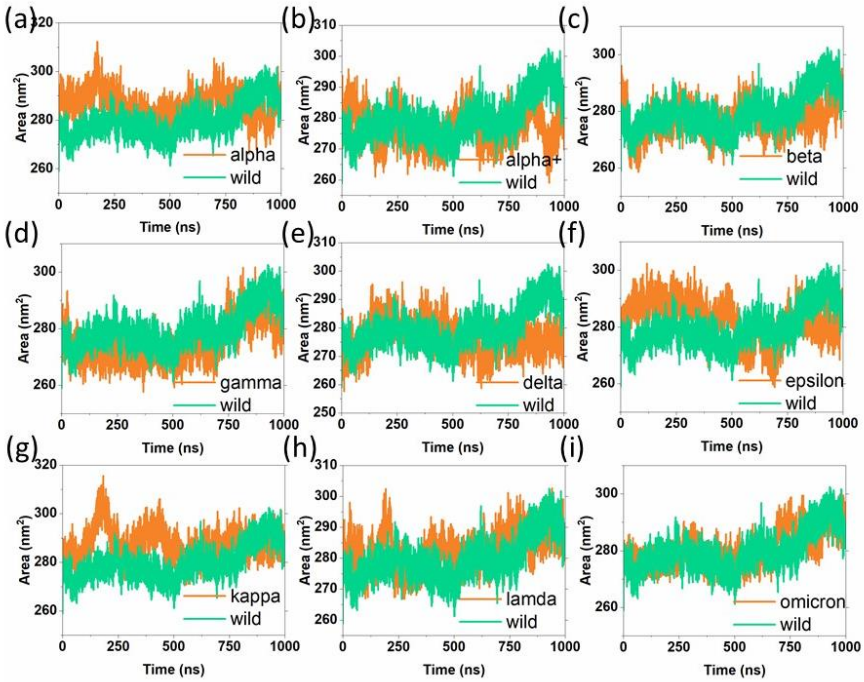

Figure S12. The time-dependent solvent accessible surface area for ACE2 receptors.

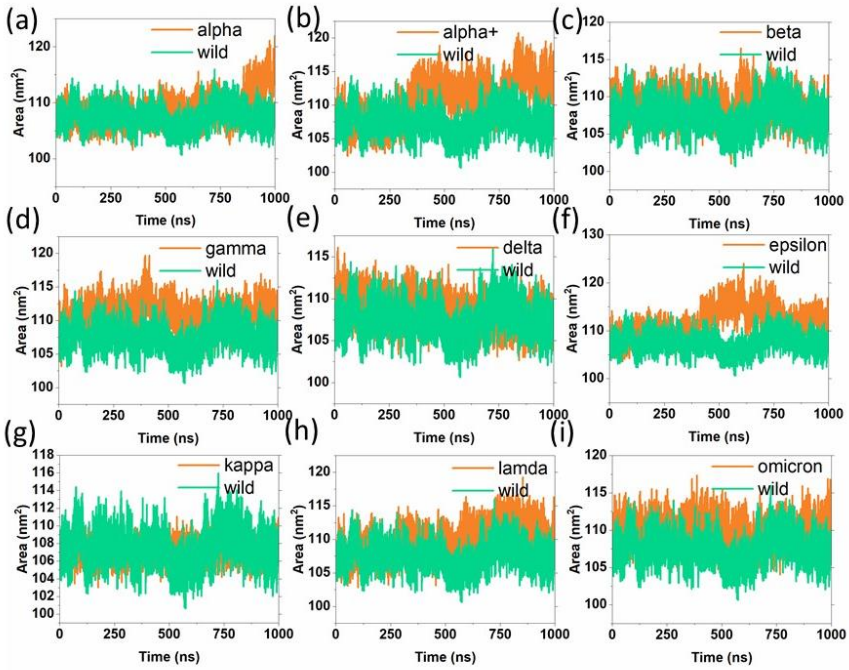

Figure S13. The time-dependent solvent accessible surface area of RBD wild and its mutants.

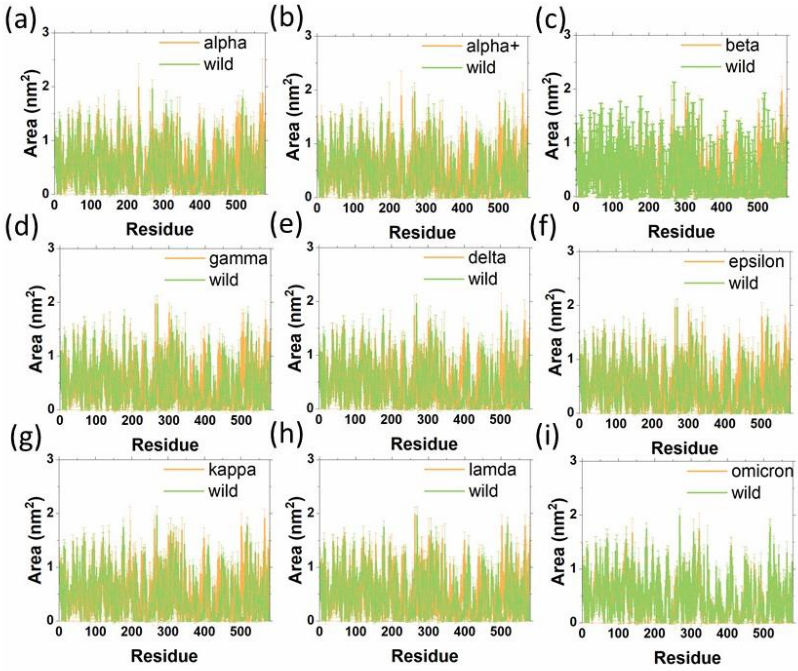

Figure S14. The residue-wise solvent accessible surface area of ACE2 receptors.

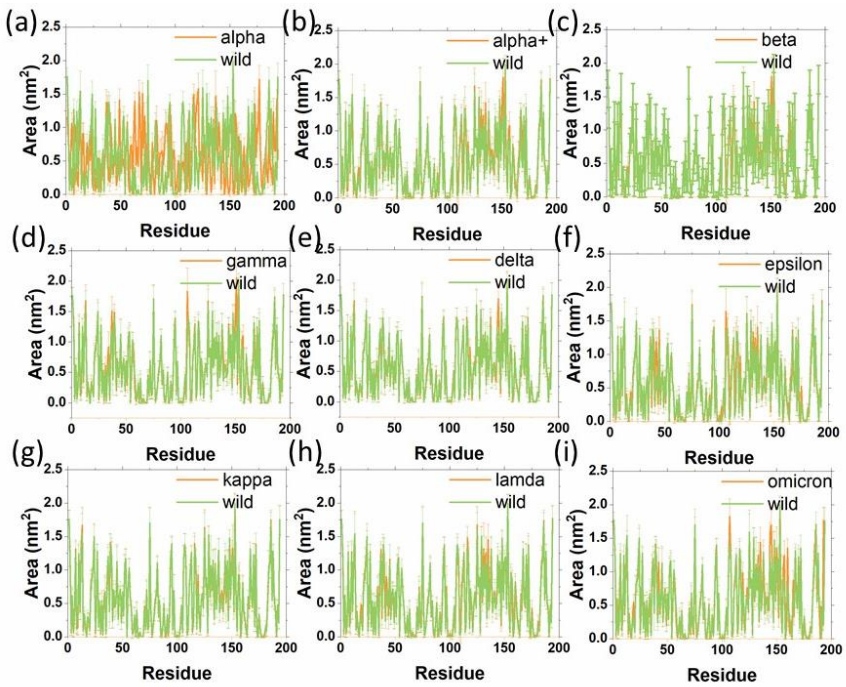

Figure S15. The residue-wise solvent accessible surface area of RBD and its mutants.

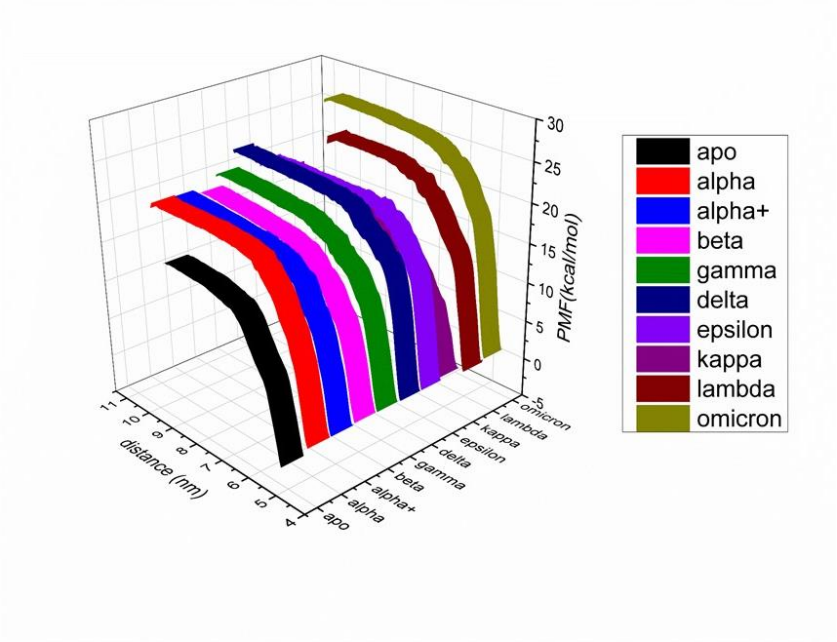

Figure S16. The potential of mean force of ACE2-RBD wild and mutants.

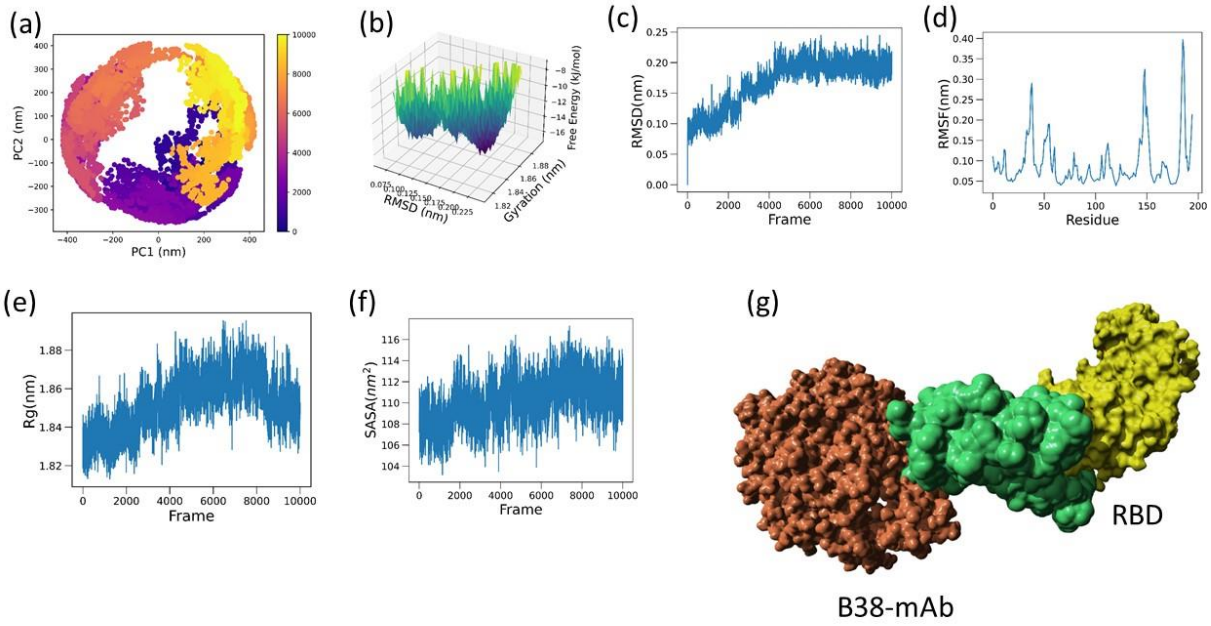

Figure S15. (a) represents the PCA of RBD that is bound with antibody and (b) represents the free energy landscape of RBD obtained from RMSD of backbone atoms (c) and radius of gyration (e). The RMSF of Cα atoms and 3D structural representation of B38 antibody-bound RBD are given in (f) and (g) respectively.

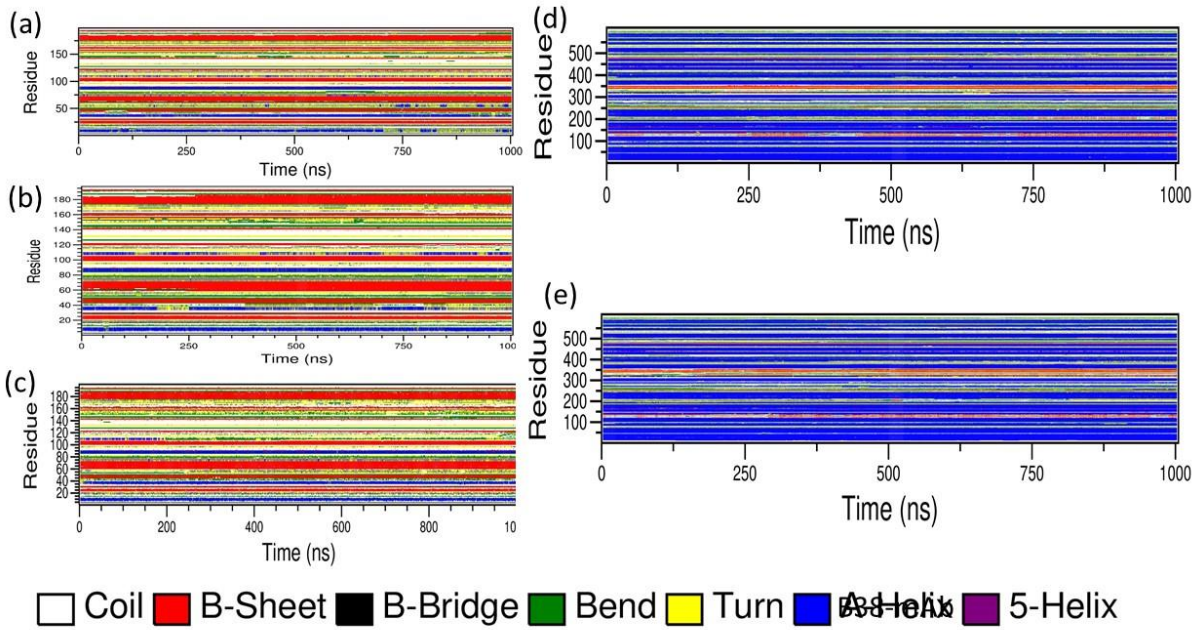

Figure S16. The time-dependent secondary structural changes of RBD (a) wild (b) antibody bound and (c) ACE2 bound RBD that inhibited by the antibody. (d) and (e) represents the time defendant secondary structural changes of wild ACE2 receptor and that bound with inhibited RBD.

	Helix (%)	Sheet (%)	Turn (%)	Coil (%)	3_{10} Helix (%)
Wild	6.2	30.9	17.5	42.3	3.1
Alpha	7.7	28.9	17.5	45.9	
Alpha+	6.2	26.3	24.7	42.8	
Beta	6.2	26.8	22.2	44.8	
Gamma	3.1	28.4	20.6	45.9	2.1
Delta	6.7	33	19.1	38.	3.1
Epsilon	10.3	27.3	17.5	42.8	2.1

Kappa	6.2	29.4	13.9	47.9	2.6
Lambda	6.7	30.9	25.8	36.6	
omicron	9.3	32.6	22.3	35.8	

Table S17. The percentage of the secondary structure after 1 µs simulations of ACE2 receptor.